AGILIS: Restoring Functional Grasping in Individuals with Tetraplegia using Epineural Electrodes

Christine Azevedo Coste, Charles Fattal, Lucie William, *Member, IEEE*, Lucas Fonseca, *Member, IEEE*, Arthur Hiairrassary, David Andreu, Antoine Geffrier, Jacques Teissier and David Guiraud, *Member, IEEE*

***Abstract*— We propose a novel approach to restore grasping in individuals with complete tetraplegia using epineural stimulation. Two multi-contact cuff electrodes were positioned around radial and median nerves in 2 volunteers during a surgery. The electrodes were maintained for 28 days. A user interface allowed triggering pre-programmed stimulation sequences on demand by executing stereotyped movements or by contracting voluntarily muscle on the contralateral shoulder. The stimulation selectivity obtained with the epineural electrodes was sufficient to obtain functional palmar and key pinch grip.**

***Index Terms*—Functional Electrical Stimulation (FES), Tetraplegia, Neural electrodes.**

I. Introduction

Functional electrical stimulation (FES) is a means of restoring upper limb function in people with complete tetraplegia when functional tendon surgery or nerve transfer is not an option [1].

Intramuscular and epimysial electrodes have been used in the past to restore grip [2,3]. A disadvantage of this approach is the need for one electrode and one cable per muscle to be activated. Miniature, self-contained implant designed to be injected in or near muscles have also been proposed to avoid cables [10].

In the AGILIS approach, we propose to use 1 epi-neural electrode per nerve to activate the different muscles to reduce the number of implanted electrodes [4]. The cuff electrodes were designed to be self-adjusting to nerve diameter.

The objectives of the study we present here were to: 1) evaluate the safety of the procedures of implanting 2 cuff electrodes around the median and radial nerves respectively and maintaining them for 28 days, 2) evaluate the ability of the solution to elicit a functional grip in two participants with complete tetraplegia.

Christine Azevedo Coste is with Inria, University of Montpellier, France (e-mail: Christine.Azevedo@inria.fr), (https://orcid.org/0000-0002-7379-8004)

Charles Fattal is with Rehabilitation Center Bouffard-Vercelli USSAP, Perpignan, France, (https://orcid.org/0000-0002-3042-0941)

Lucie William with Inria, University of Montpellier, France,

Lucas Fonseca is with with Inria, University of Montpellier, France, (https://orcid.org/0000-0002-7255-5916)

Arthur Hiairrassary is with Neurinnov, Montpellier, France.

David Andreu is with Neurinnov, Montpellier, France.

Antoine Geffrier is with University Hospital Center Pontchaillou, Rennes, France. He was previously with APHP, Paris France.

Jacques Teissier is with Surgical Clinic OrthoSud, Montpellier, France.

David Guiraud is with Inria, University of Montpellier, France and Neurinnov, Montpellier, France.

II. Methods

Two volunteers with complete C4 tetraplegia, AIS A were included. They signed an informed consent. The study was approved by the National Ethics Committee (ClinicalTrials.gov ID NCT04306328).

The electrodes were placed during an initial surgical procedure and explantation surgery took place 28 days later. 2 multi-contact spinal electrodes (CorTec GmbH Freiburg Germany) were wrapped around the nerves above the elbow. Each electrode was connected to a percutaneous cable to connect the multi-source external stimulator (STIMEP, INRIA, Montpellier) [8]. The stimulator was controlled from a computer (Figure 1).

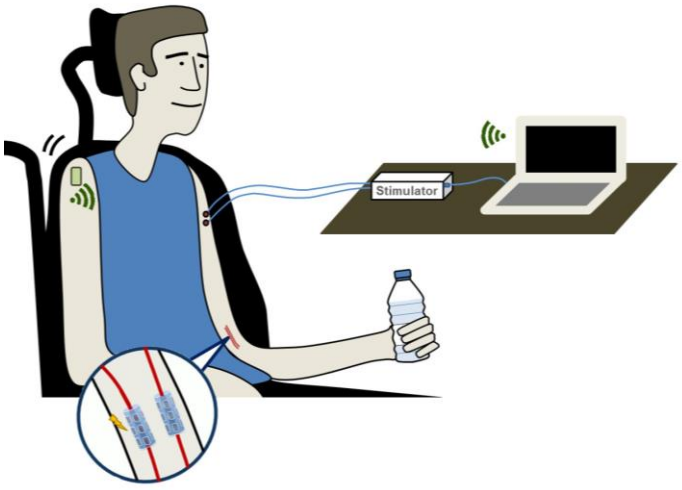

Fig. 1. AGILIS approach principle: 2 multi-contact cuff electrodes are wrapped around radial and median nerves. Percutaneous cables are connected on demand to an external pulse generator. Stimulation configuration patterns are pre-programmed to elicit hand opening/closing. The user controls contralateral shoulder movements or muscle contraction to send commands to the stimulator software: hand opening, palmar or key pinch grip…

Two control interfaces were tested to allow the user to trigger the pre-programmed stimulation patterns: 1) the participant used stereotyped voluntary shoulder movements of the contralateral limb captured by 1 IMU, 2) the participant used voluntary contractions of 2 muscles of the contralateral limb

 ISBN 978-86-7466-930-3

captured by 2 EMGs (trapezius and platysma). A finite state machine (FSM) was defined to associate user commands (EMG threshold detection or predefined movement recognition (IMU)) with actions depending on the current state of the FSM [6].

Various measurements were made wireless sensors (Delsys, Natick, MA) and offline processed using: electromyography (EMG), forces applied to objects (resistive force sensors (FSR)), movements (inertial measurement units (IMU)). The kinematics of the movements were also analysed (Leap Motion, Inc, San Francisco, California). FES-induced evoked muscle contractions (eEMG) were also acquired and post-processed to extract recruitment curves [9].

III. Results

Both participants were able to perform object grasping tasks using two types of grasp (key pinch and digito-palmar). Participant 1 was able to use both control interface modalities (muscle contraction and voluntary movements). Participant 2, due to a significant fatigability of the shoulder muscles, was able to use only voluntary shoulder movements to trigger the stimulation sequences, but in a rather non-robust manner, which led us to propose a third solution based on occipital contactors. Some results have been published in a recent article [7]. Additional results will be detailed during the presentation at the conference.

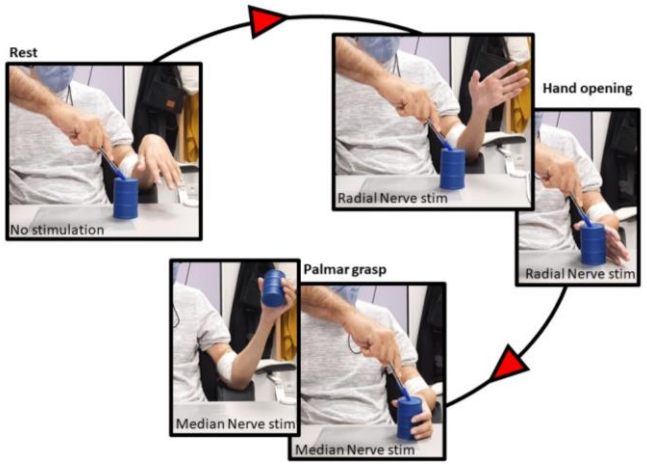

Fig. 2. Example of a sequence of movements for gripping a foam cylinder. The participant triggers the stimulation of the radial nerve which causes the hand to open (extension of fingers and wrist), he positions his hand on the object and then triggers the stimulation of the median nerve which causes the fingers to close around the object which he can then move.

IV. Conclusion

This preliminary study is a further step in the validation of the AGILIS approach which suggests the feasibility of a solution for grip restoration that minimises surgical complexity. Less than 2 hours were required to place the 2 multi-contact epineural electrodes with percutaneous cables around the radial and median nerves. These two electrodes associated with the electrical stimulator allow the injected currents to be controlled to achieve selective activation of the nerve fascicles. Two separate taps could be activated and associated with reproducible configurations (active electrode poles and stimulation parameters). The behaviour of the electrodes remained stable during the implantation period (28 days). Further studies are needed to strengthen the results.

Acknowledgment

The authors would like to thank the two volunteers, as well as Mrs Caralp and Mrs Porra (OT), Mr Panel and Mr Ferrer (PT), and the health care teams responsible for daily care. This study was supported by grants from the EIT Health, the Occitanie Region and the ERC MSCA.

References

[1] van Zyl, N., Hill, B., Cooper, C., Hahn, J., and Galea, M.P. Expanding traditional tendon-based techniques with nerve transfers for the restoration of upper limb function in tetraplegia: a prospective case series. *Lancet* 394, 565–575, 2019.

[2] Hoshimiya, N., and Handa, Y. A master-slave type multi-channel functional electrical stimulation (FES) system for the control of the paralyzed upper extremities. *Automedica*, 209–220, 1989.

[3] Keith, M.W., Peckham, P.H., Thrope, G.B., Stroh, K.C., Smith, B., Buckett, J.R., Kilgore, K.L., and Jatich, J.W. Implantable functional neuromuscular stimulation in the tetraplegic hand. *J Hand Surg Am* 14, 524–530, 1989.

[4] Tigra, W., Dali, M., William, L., Fattal, C., Gélis, A., Divoux, J.-L., Coulet, B., Teissier, J., Guiraud, D., and Azevedo Coste, C. Selective neural electrical stimulation restores hand and forearm movements in individuals with complete tetraplegia. *J Neuroeng Rehabil*, 2020.

[5] Tigra, W., Navarro, B., Cherubini, A., Gorron, X., Gelis, A., Fattal, C., Guiraud, D., and Azevedo Coste, C. A Novel EMG Interface for Individuals with Tetraplegia to Pilot Robot Hand Grasping. *IEEE Trans Neural Syst Rehabil Eng* 26, 291–298, 2018

[6] Fonseca, L., Tigra, W., Navarro, B., Guiraud, D., Fattal, C., Bó, A., Fachin-Martins, E., Leynaert, V., Gélis, A., and Azevedo-Coste, C. Assisted Grasping in Individuals with Tetraplegia: Improving Control through Residual Muscle Contraction and Movement. *Sensors (Basel)*, 2019.

[7] Fattal C., Teissier J., Geffrier A., Fonseca L., William L., Andreu D., Guiraud D., Azevedo-Coste C. Restoring Hand Functions in People with Tetraplegia through Multi-Contact, Fascicular, and Auto-Pilot Stimulation: A Proof-of-Concept Demonstration. *Journal of Neurotrauma*, 2022.

[8] Guiho T., López-Alvarez V., Cvancara P., Hiairrassary A., Andreu D., Stieglitz T., Navarro X., Guiraud D., New Stimulation Device to Drive Multiple Transverse Intrafascicular Electrodes and Achieve Highly Selective and Rich Neural Responses, *Sensors*, 2021.

[9] William L., Dali M., Azevedo Coste C., Guiraud D. A method based on wavelets to analyse overlapped and dependant M-Waves, *Journal of Electromyography and Kinesiology*, 2022.

[10] Popovic D, Baker LL, Loeb GE. Recruitment and comfort of BION implanted electrical stimulation: implications for FES applications. IEEE Trans Neural Syst Rehabil Eng. 2007.

 ISBN 978-86-7466-930-3

A Device for Monitoring Physiological Parameters and Electrotactile Stimulation

Bojan Jorgovanović, Matija Štrbac, Miloš Kostić, Vojin Ilić, Nikola Jorgovanović

***Abstract* — This work stems from a research and innovation action financed under Secure societies programme of the European Union's Horizon 2020 framework. Specifically, the aim is to develop an easy-to-use wearable system for enhancing situational awareness of first responders deployed in extreme environments by providing tactile feedback on the risk factors that can lead to rapid deterioration of their health or operation capabilities. For this purpose, an unobtrusive system was designed to acquire, process, and analyse the data from a battery of novel biosensors and generate actionable information about assessed health risks, in real-time. Aptly named SIXTHSENSE, it leverages electrotactile stimulation to continually convey this information to the first responder wearing it, leveraging the sense of touch. It effectively expands first responders' sensory bandwidth to include the "feeling" of changes in critical parameters that are not within the reach of human senses, like the ionic imbalance, the lactate level or physiological strain, much before they manifest through symptoms of exhaustion, heatstroke or hypothermia. The developed system further incorporates means for transmitting information to the command centre, where it can be analysed and visualised through a mission specific decision support system, allowing for a more efficient and safer data-driven team management.**

***Index Terms*—Electrotactile stimulation; First responders; Wearable acquisition unit**

I. Introduction

SIXTHSENSE is a multidisciplinary innovation and research action with the overall aim to significantly improve efficacy and safety of first responders' deployment in hazardous environments by optimising on-site team coordination and mission execution.

Bojan Jorgovanović is with the Faculty of Technical Sciences, University of Novi Sad, Trg Dositeja Obradovića 6, 21000 Novi Sad, Serbia and Global Electronic Solutions doo, Cara Dušana 75, 21000 Novi Sad, Serbia (e-mail: bojan.jorgovanovic@uns.ac.rs).

Matija Štrbac is with Tecnalia Serbia doo, Deligradska 9, 11000 Belgrade, Serbia (e-mail: matija.strbac@tecnalia.com).

Miloš Kostić is with Tecnalia Serbia doo, Deligradska 9, 11000 Belgrade, Serbia (e-mail: milos.kostic@tecnalia.com).

Vojin Ilić is with the Faculty of Technical Sciences, University of Novi Sad, Trg Dositeja Obradovića 6, 21000 Novi Sad, Serbia and Global Electronic Solutions doo, Cara Dušana 75, 21000 Novi Sad, Serbia (e-mail: vojin@uns.ac.rs).

Nikola Jorgovanović is with the Faculty of Technical Sciences, University of Novi Sad, Trg Dositeja Obradovića 6, 21000 Novi Sad, Serbia and Global Electronic Solutions doo, Cara Dušana 75, 21000 Novi Sad, Serbia (e-mail: nikolaj@uns.ac.rs).

Between the booming EU economy and the climate change, the number and consequences of disasters occurring in inaccessible rural areas is on a constant rise. First responder deployments in extreme conditions such as fighting wildfires or alpine search and rescue missions have gone from exceptional to regular events in only a couple of decades. As this trend is likely to continue, the risks for wellbeing of the engaged first responders continue to grow. To avoid the loss of life or lasting consequences on the first responders' health, it is important that the key physiological parameters of deployed operatives are monitored in a way that provides timely and actionable information, without hindering their operational capacity [1]. One way to achieve gathering such data and providing feedback is to use a device which could monitor the first responder's physiological parameters and use electrotactile stimulation as a way of conveying a message [2, 3].

At this point, a device that could do both data acquisition and analysis and give feedback to the first responder via stimulation is not available on the market, so it was necessary to develop one. The device presented in this paper is named the Alpha Mobile Device (AMD). The AMD is a system for multimodal data acquisition and control of electrotactile feedback stimulation. The aim of the AMD design was to enable synchronised electrotactile stimulation and acquisition from multiple sensors in a modular and scalable way that enables the inclusion of existing, developed and emerging sensors. The AMD design provides compactness, low power consumption, small overall dimensions and robustness with a main goal to develop a real mobile and wearable system.

II. Architecture of the AMD

The AMD was based on the STM32H743VIT6 microcontroller by ST Microelectronics. This ARM microcontroller has plenty of integrated peripheral modules which can work with very little or no processor core supervision. Furthermore, the STM32H743VIT6 microcontroller includes enhanced power management which provided all necessary power down or sleep operating modes in order to reduce power consumption.

The AMD needed to encompass 3 functionalities - data acquisition, electrotactile stimulation and communication. A block diagram of the AMD is shown in Figure 1.

 ISBN 978-86-7466-930-3

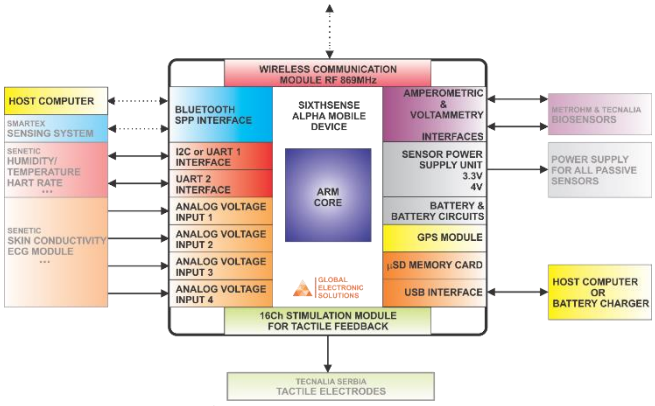

Figure 1. Block diagram of the AMD

A. Data acquisition

The AMD is equipped with interfaces for acquisition data from following type of sensors:

- Analog sensors with voltage output
- NTC thermistor sensor for temperature measurement
- Electrochemical sensors – Biosensors
- Digital wired sensors with USART interfaces
- Digital wired sensor with I2C interface
- Wireless connected sensor system with Bluetooth SPP interface
- GNSS sensor

The AMD is equipped with four voltage analogue inputs. Analogue voltage input 1 is also equipped with a precise current source which provides a constant current flow of 100µA to pin 13 of the sensor connector. This construction allows temperature measurement using the precise 10kΩ NTC thermistor connected between analogue ground and AIN_0. The other three analogue inputs are standard voltage inputs. By default, all four analogue inputs are connected to the internal 16-bit ADC of the microcontroller with a sampling rate of 1KSPS. If it turns out that the accuracy of the internal ADC is not satisfactory each input can be independently rerouted to a high speed and high accuracy ADC of the AD5941 by SMD jumpers on the PCB.

The AMD is equipped with two inputs for electrochemical sensors (biosensors). This interface is based on the single channel electrochemical front end circuit, AD5941, by Analog Devices. The electrochemical sensor interface can be set to operate in the following modes:

- Amperometric
- Chronoamperometric
- Cyclic Voltammetry

B. Electrotactile stimulation

This functionality is intended for conveying messages to the first responder wearing the device through electrotactile stimulation. The device is designed to be compatible with multi-pad electrodes [4] designed and produced by Tecnalia Serbia doo. The AMD stimulation unit consists of the following blocks:

- DC/DC step-up voltage converter
- Biphasic current source
- Switch area (output demultiplexer)
- Control unit
- Battery and interfaces

The purpose of the DC/DC step-up converter is to provide voltage which is high enough to enable current flow through relatively high electrode-skin interface impedance. The manufactured DC/DC converter for the AMD is capable to boost battery voltage to voltage a level of up to 150V. This converter is based on a modified boost topology with coupled coils, and this design is confirmed in a number of different electrical stimulators previously developed by Global Electronic Solutions. The converter output voltage can be pre-set by the programme of the control unit. This flexibility is very important especially for the Alpha system in order to find the optimal voltage level in real life tests.

Biphasic Current source is based on current controlled H-bridge topology which is capable to create an either monophasic or biphasic current pulse. The amplitude of the current pulse is controlled by a control loop which is integrated into the H-bridge. This approach reduces the number of components and overall module dimensions. The set-point of the pulse amplitude is set by the control unit via a 16-bit D/A converter with standard SPI interface.

The Switch area includes a high-voltage switching circuit that allows multiplexing a signal from the H-bridge and driving it to one or more of the 16 output channels. Only one pole of the current source (cathode) can be distributed to any of the 16 electrode pads while the other pole (anode) is connected to a single predefined electrode pad, known as the unipolar stimulation topology.

The Alpha prototype will be based on ST Electronics' high performance ARM microcontroller (MCU). Only a small part of this microcontroller's resources are intended for the operation of the stimulator subsystem, while a bigger part will be used for the sensor data acquisition module. According to that, the part of the MCU which acts as the Stimulator control unit has the following important functionalities:

- Stimulation pulses waveform timing control
- Stimulation pulses amplitude control
- Stimulation pulse distribution to the pads of the multi-pad electrode
- Execution of the predefined electrotactile stimulation schemes

Beside the subsystems intended exclusively for the stimulator subsystem, there are two other common parts of the Alpha prototype which are necessary for the functioning of the stimulator subsystem and those parts are also integrated in the realized stimulator prototype:

- Battery and a battery electronic circuit
- Communication interfaces

The manufactured prototype is powered by Li-poly rechargeable battery. Battery charging, battery protection and battery monitoring electronic circuits are an integral part of the stimulator prototype. The manufactured device has Bluetooth

 ISBN 978-86-7466-930-3

and isolated USB interfaces. The following functionalities are realized via both communication channels:

- Setting all stimulation parameters (pulse width, pulse rate, pulse amplitude, active output channels)
- Starting/Stopping the stimulation
- Creating stimulation schemes
- Programming via a bootloader application

The device is also equipped with two multicolour LEDs indicating battery status, communication and stimulator activity. A block diagram of the stimulator is shown in Figure 2.

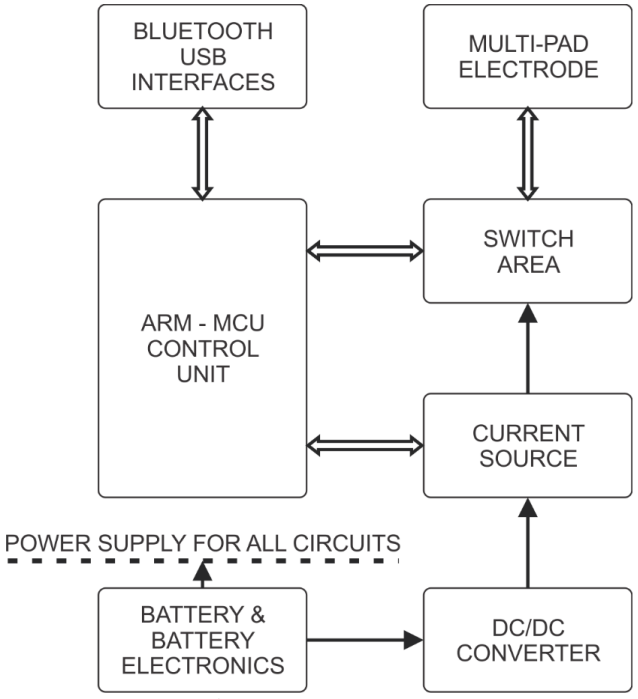

Figure 2. Block diagram of the AMD stimulator

C. Communication

The AMD is equipped with a narrow band RF communication channel for duplex communication between the first responder and the command centre. The communication is based on the GES-RF869 communication module produced by Global Electronic Solutions. The GES-RF869 is a radio module which is in compliance with ETSI EN 300 220-1. This module provides the possibility of exchanging small packets of data, up to 100 Bytes, with low speeds, in a relatively simple way. It works on an operational frequency band ranging from 869,400MHz-869,650MHz which enables it to have radiated power of up to 27dBm (500mW). It provides duty cycle control and obeys the 10% duty cycle restrictions for the 869,400MHz-869,650MHz frequency band. It offers multiple radio communication channels inside the operational frequency band and the possibility of configuring the transmit power. In order to optimize power consumption and communication range the transmit power can be set between 10mW and 500mW. The ISM standalone antenna by Molex is integrated inside of the AMD enclosure.

III. Results

The stimulator was tested on a circuit which resembles the electronic properties of the electrode-tissue interface and the signals were recorded using an oscilloscope. The waveform of the stimulation current is recorded at the serial resistor R_S by voltage input of the oscilloscope. The resistance of R_S is 1kΩ, so 1V at the recorded waveform corresponds to 1mA of measured current. A block diagram of the equipment used for testing the stimulator is shown in Figure 3.

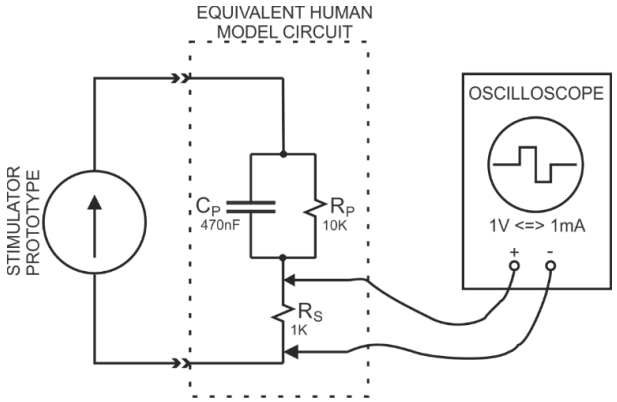

Figure 3. Block diagram of the test equipment

The waveform of a biphasic pulse generated by the AMD stimulator is shown in Figure 4. The pulse width of the generated stimulation pulse is 250µs, and the amplitude is 5mA.

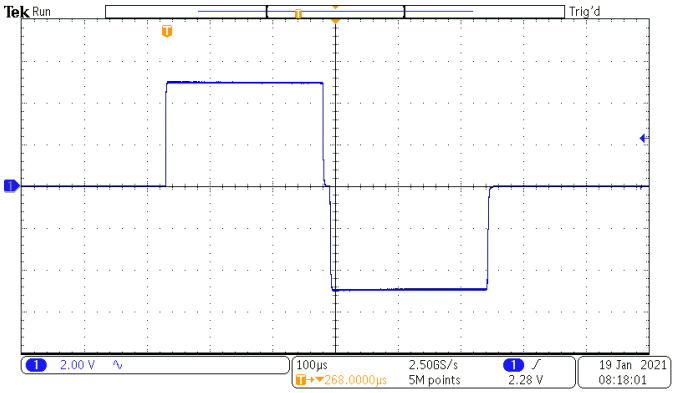

Figure 4. Stimulation pulse biphasic charge compensated test

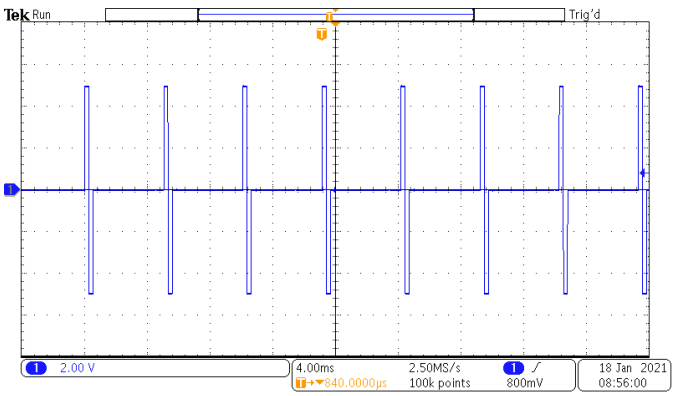

Figure 5. Stimulation pulse train

 ISBN 978-86-7466-930-3

A stimulation pulse train generated by the AMD stimulator is shown in Figure 5. The frequency of the pulse train is 200pps and each pulse has the same stimulation parameters as the pulse shown in Figure 4.

IV. Conclusion

The AMD device was designed and produced for the purposes of the SIXTHSENSE project. It has since been successfully tested in two field trials performed by first responders. The functionality of acquiring data was used for collecting physiological data about the first responders from various sensors. These data were both logged on an integrated µSD card and transmitted to a command centre which was realised through the communication functionality. Through electrotactile stimulation, the first responders were notified if certain parameters were out of regular boundaries. Feasibility tests in the field trials proved that the realized specifications of the voltage converter and the current source provided a sufficient range of stimulation levels for the tactile communication over multi-array electrodes placed on the torso of the user during physical activity, i.e. skiing and walking. The accuracy of the stimulation pulses shown in Figures 4 and 5 is satisfactory for electrotactile stimulation and the pulse amplitude error with respect to the set point value is negligible. Furthermore, initial tests proved that flexibility provided through the creation of stimulation patterns, which consider change of the active electrode pad and stimulation frequency, allow the generation of a large number of feedback messages. Given the number of different interfaces integrated in the device, it can also be used outside the scopes of the SIXTHSENSE project. The mentioned interfaces allow the device to communicate with both analogue and digital sensors of many types which makes it suitable for different kinds of tests and experiments. Furthermore, the powerful STM32H743VIT6 microcontroller used as the core of the device can even be used for certain signal processing applications or for running more complex algorithms than the ones used in this project.

Acknowledgment

This work has received funding from the European Union's Horizon 2020 research and innovation programme under grant agreement No 883315.

References

[1] R. Gasaway, Situational Awareness for Emergency Response, 2013.

[2] M. A. Garenfeld, N. Jorgovanović, V. Ilić, M. Štrbac, M. Isaković, J. L. Dideriksen and S. Došen, "A compact system for simultaneous stimulation and recording for closed-loop myoelectric control," *Journal of NeuroEngineering and Rehabilitation,* 2021.

[3] M. Štrbac, M. Isaković, J. Malešević, G. Marković, S. Došen, N. Jorgovanović, G. Bijelić and M. Kostić, "Electrotactile Stimulation, A New Feedback Channel for First Responders," 2021.

[4] A. Popović-Bijelić, G. Bijelić, N. Jorgovanović, D. Bojanić, M. B. Popović and D. B. Popović, "Multi-Field Surface Electrode for Selective Electrical Stimulation," 2005.

 ISBN 978-86-7466-930-3

Deep Neural Network Approach for Artifact Detection in Raw ECG

Tanja Boljanić, Jovana Malešević, Goran Kvaščev

***Abstract*—Electrocardiography is a non-invasive technique for monitoring the electrical activity of the heart, and its analysis can detect and then prevent many health problems. Alterations that are not related to cardiac electrical activity represent artifacts in signal and should be minimized in order to correctly interpretate the signal. This is of great importance in wearable systems for electrophysiological monitoring that have numerous applications in healthcare and fitness. This paper presents how to build a classification model to detect artifacts in electrocardiogram (ECG) signal using deep neural network. The Long Short-Term Memory (LSTM) network was proposed for classifying 10-s single-channel ECG segments as *Valid* and *Artifact.* Data set consists of 10,231 raw ECG samples. The results show that the proposed method can classify the data with the accuracy of 90.1%, i.e., efficiently deal with acceptance of good (93.8%) and rejection of poor (80.1%) ECG quality.**

***Index Terms*—ECG; Deep Neural Network; LSTM, Classification Model**

I. Introduction

ELECTROCARDIOGRAPHIC (ECG) artifacts are alterations that are not related to cardiac electrical activity. The artifacts could be caused by the unexpected motion intensity, loss of electrode-skin contact or movements of different part of the system such as cables. Additionally, some of the common noises that appear in the ECG signal are electromyogram (EMG) noise and baseline drift due to breathing or sudden movement, and such noises can be easily removed using various filtering approaches. The problem occurs if the artifacts last too long, and completely compromise the shape of the signal. Then, the current physical state of the subject could be misinterpreted. That is why it is of great importance to identify these types of artifacts and ignore the parts of the signal in which they appear. This is especially referring to the wearable systems for electrophysiological monitoring that are used for healthcare or fitness where health condition of the subjects is further decided based on the parameters extracted from the ECG signal. Since the subjects perform various physical activity, the quality of the ECG signal even more decreases. As predictions of the physical state are given in the real time, the artifacts detection as well as the other algorithms should be performed automatically.

Lui et al. [1] developed a wearable system for early detection of cardiovascular diseases and used machine learning algorithm for classifying ECG segments as acceptable and unacceptable for further analysis. Using Support Vector Machine (SVM), they could exclude unacceptable segments with an accuracy of 96.4%.

Neural networks are widely used for classification of different types of artifacts or arrhythmias in ECG signal [2-7]. Saadatnejad at al. [2] proposed a method consisting of wavelet transform and multiple recurrent neural networks for classifying arrhythmias in continuous cardiac monitoring on wearable devices. Deep network with wavelet sequences as input was used for classification of five heartbeat signals, resulting in high recognition performance [3]. Six common types of urgent arrhythmias are classified using deep neural network with an overall accuracy of 81% [4]. Deep learning algorithms were also used to classify shockable versus non-shockable rhythms in the presence and absence of cardiopulmonary resuscitation (CPR) artifact for automated external defibrillators [5]. Chauhan and Vig used deep recurrent neural network architecture with Long Short Term Memory (LSTM) units to detect abnormal and normal signals in ECG data [6]. The data included four different types of abnormal beats and the proposed detection system provided 96.5% performance.

The aim of the presented work is to develop a system that can automatically identify artifacts in ECG signals. We propose deep learning method for classification of unwanted artifacts and ECG signal that could be further processed, as we believe that these differences in signal could be reliably detected by a properly trained neural network.

Section II contains the method, including data preparation, and an explanation of used algorithm with the configuration of its parameters. The results are presented and discussed in section III, while the conclusion is attached in the final section.

II. The Method

The proposed algorithm is implemented in the Matlab R2019b software installed in a Windows 10 Pro platform, using the Signal Processing and Deep Learning toolboxes. The computer that was used is equipped with NVIDIA GeForce RTX 3060 graphics processing unit.

A. Dataset and Implementation

Dataset that was used in this study was collected by Tecnalia Serbia during the field trials within SIXTHSENSE

Tanja Boljanić and Goran Kvaščev are with the School of Electrical Engineering, University of Belgrade, 73 Bulevar kralja Aleksandra, 11020 Belgrade, Serbia (e-mail: tanja.boljanic@gmail.com)

Tanja Boljanić and Jovana Malešević are with the Tecnalia Serbia Ltd, Deligradska 9, 11000 Belgrade, Serbia

 ISBN 978-86-7466-930-3

project [8] in Bormio, Italy. The sensing module based on a multi-electrode array (MEA) for ECG recording was placed below the left major pectoralis. The MEA contains two recording and one referent electrode. The module provides conditioning and A/D conversion of the signal, and it is connected to the sensor for data acquisition via the flat cable. Described prototype was developed for research purposes within the project. This dataset comprises one-lead ECG recordings from 12 mountain rescuers that were performing the rescue task (male/female, 11/1, age (mean ± std), 31.7 ± 6.0 year). The length of the ECG signals ranges from 90 to 200 min with the average of 150 min, and the sampling rate is 1000 Hz. The signal contains motion artifacts due to the unexpected motion intensity and motion state, and the noises due to the change of relative displacement between electrode and skin, as well as the artifacts due to the cable movements. These noises have typical characteristics as transient high amplitude impulse and signal saturation. In order to utilize the automatic identification of the artifacts in signal, the ECG was visually inspected and we manually selected segments that are extremely noisy.

All signals were divided into 10-s segments, with total of 7,517 valid ECG and 2,714 segments labeled as signal with artifacts (7,517 + 2,714 = 10,231). Artifact segments are selected so that more than a half of the segment contain pure noise resulting in visually undetectable QRS complexes. An example of signal's both classes is presented in Fig. 1.

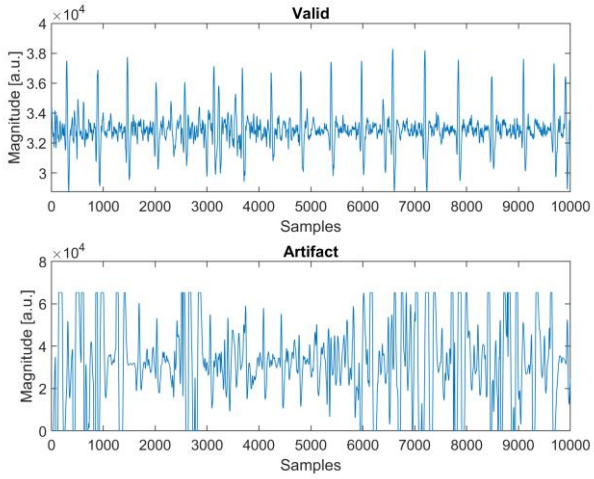

Fig. 1. The example of 10-s ECG segments: a segment without artifacts (*Valid*, top) and a segment with artifacts (*Artifact*, bottom)

The raw data segments were divided into two sets: 90% and 10% for the training and testing, respectively. Both classes were randomly divided into these two sets. Since 73.5% of the dataset are valid segments, a classifier would learn that it can achieve a high accuracy simply by classifying all signals as *Valid*. To avoid this bias, the *Artifact* signal was augmented so that there is the same number of *Valid* and *Artifact* signals. This is one form of data augmentation used in deep learning, known as oversampling [9]. *Artifact* signals were augmented after splitting data into two sets, hence the data from the test set are not included in the training set. At the end, the distribution between *Valid* and *Artifact* signals was evenly balanced, as showed in Table I.

B. *Proposed Deep Neural Network*

Deep Neural Networks (DNN) are one type of model for machine learning that is subfield of artificial inteligence (AI) [10]. The appropriate deep learning algorythm depends on the task and the available data. Long short-term memory (LSTM) networks are the most commonly used variation of recurrent neural networks (RNN) that are well situated to study sequence and time-series data [11].

TABLE I
THE DIVISION OF THE ENTIRE DATASET INTO TRAINING AND TESTING SETS

Classes	The original number of 10-s segments	Number of 10-s segments after leveling	
		Training	Test
Valid	7,517	6,765	752
Artifact	2,714	6,765	271

The LSTM network can effectively learn long-term relationships between time steps of a sequence. It consists of an input gate, forget gate, output gate and cell unit. The cell remembers values over arbitrary time intervals, and the gates regulate the flow of information into and out of the cell. Input gate protects the unit from irrelevant input events, while the forget gate controls when to forget previous memory contents. The output gates controls the output flow. Graphical representation of an LSTM unit is presented in Fig. 2. The LSTM network can look at the time sequence in the forward direction and in both forward and backward directions, which is than called bidirectional LSTM (BiLSTM). This is useful when there is need to learn from the complete time series at each time step.

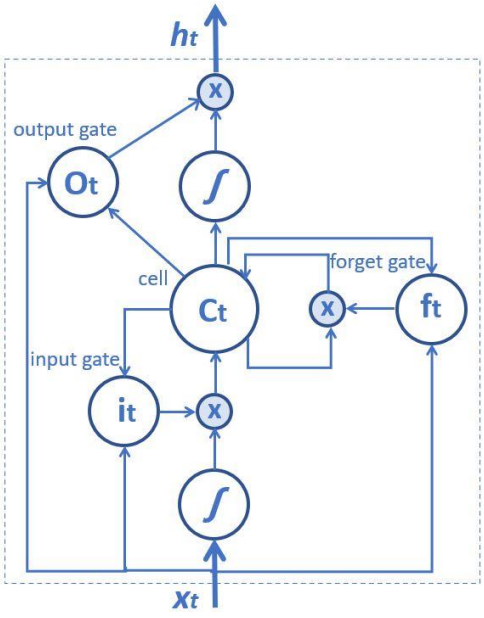

 ISBN 978-86-7466-930-3

Fig. 2. LSTM block diagram. The variables are: x_t – input vector to the LSTM unit, i_t – input gate's activation vector, f_t – forget gate's activation vector, o_t – output gate's activation vector, c_t – cell state vector, h_t – output vector of the LSTM unit.

C. Network Parameter Configuration

LSTM network was proposed for ECG classification. The network parameters were selected experimentally or following the other studies [9,12,13]. The bidirectional LSTM (BiLSTM) with 200 hidden units was used, as it looks at the sequence in both directions – backwards and forward, which is important when network should learn from full-time series at each time step. Sequence input was set to one dimension, because the input signal is only the amplitude of raw ECG. Two classes were specified by including a fully connected layer of size 2. The last two layers were softmax and classification layer with cross-entropy loss function. The adaptive moment estimation algorithm (ADAM) was used as the optimization method. Architecture of a network is summarized in Table II. The layer information from the table includes the layer type, the size and format of the layer activations, and the size of learnable parameters.

TABLE II
THE DETAILED INFORMATION FOR EACH LAYER OF THE PROPOSED NETWORK MODEL

Name	Type	Activations	Learnables
input	Sequence input	1	-
BiLSTM	BiLSTM	400	InputWeights 1600x1 RecurrentWeights 1600x200 Bias 1600x1
fc	Fully Connected	2	Weights 2x400 Bias 2x1
softmax	Softmax	2	-
output	Classification Output	-	-

The BiLSTM layer has the following parameters: initial learning rate = 0.01, mini-batch size = 150, epoch = 10, gradient threshold = 1, sequence length = 1000, dropout = 0. Number of epochs in the number of passes through the training data, and increasing this number wasn't resulting in better classification accuracy. Mini-batch size is the number of signals that neural network looks at a time, while the signal is broken into smaller sequences (sequence length) so that the computer does not run out of the memory. Dropout layer was not used as the previous studies showed that it did not increase the network generalization ability [9,12].

III. Results and Discussion

The ECG data were classified using the LSTM network and performance measures of the model were evaluated using a confusion matrix. Confusion matrixes that are obtained after the training and testing process are presented in Fig. 4-5.

A row-normalized row summary represents the percentages of correctly and incorrectly classified observations for each true class, while a column-normalized column summary represents the same thing but for each predicted class. In order to report performance results for binary classification of *Valid* and *Artifact* ECG, five statistical metrics are extracted from the confusion matrix and presented in Table III: accuracy, sensitivity, specificity, precision and F1-score.

Fig. 4. Confusion matrix for the training set of the LSTM with a raw ECG. The axes labels represent the class labels, *Valid* - "v" and *Artifact* - "a".

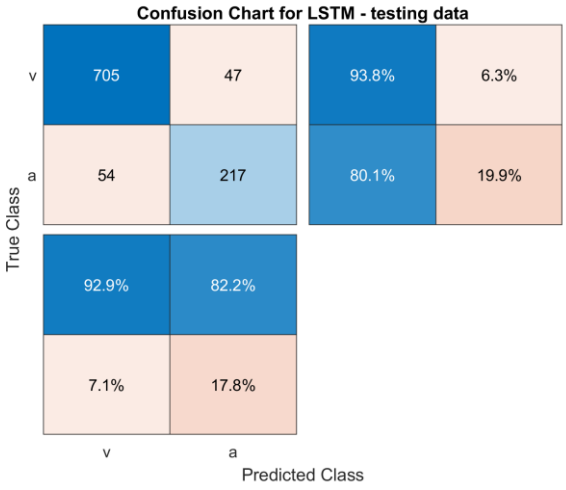

Fig. 5. Confusion matrix for the test set of the LSTM with a raw ECG. The axes labels represent the class labels, *Valid* - "v" and *Artifact* - "a".

The LSTM accuracy for the training set was 88.2%, while for the testing set it was 90.1%. The accuracy is the proportion of correctly classified ECG segments of all ECG segments. Sensitivity calculates the number of correctly classified valid ECG segments out of the total samples in the class, while the specificity calculates the number of correctly classified artifact ECG segments out of the total samples in the mentioned class. The precision calculates the number of true positives out of the positive classified classes. Finally, F1-score is the harmonic mean of both the precision and sensitivity measures and it is used as an overall score on how well the model is performing.

 ISBN 978-86-7466-930-3

TABLE III
EVALUATION METRICS FOR A CLASSIFICATION TEST

Accuracy	90.1%
Sensitivity	93.8%
Specificity	80.1%
Precision	92.9%
F1-score	93.3%

The time consumption for training was 53 min, which is acceptable, considering the large database that included more than 10,000 ECG segments (a 10-s duration for each segment). Segments of 10 seconds was used, because most of the ECG monitors display and analyze such signal duration, and Hajeb-M et al. [5] reported that 8 s segments is the best choice for classification accuracy. As mentioned in the method section, we selected the segments of ECG signal that are extremely noisy as *Artifact* signals. In practical applications, it would be of interest to observe not only the signals that are incredibly noisy, but rather signals with various degrees of noise, and it will be considered in the future work. Network parameters that are used are the optimal one for this type of dataset. Other options did not help the network to improve the classification accuracy. Some of the changes that were performed are decreasing the learning rate and the mini-batch size, and increasing the number of epochs.

The overall accuracy of 90.1% indicates that the proposed model could provide accurate prediction on a raw ECG data. By observing the sensitivity and specificity values, it can be seen that performed model recognizes valid ECG segments better than artifacts.

Similar study [9] that was also using LSTM network on raw ECG data showed the accuracy of 70.8%. Chen et al. [4] developed a classification model for six types of urgent arrhythmias combining CNN (Convolutional Neural Network) and LSTM with accuracy of 81.0%, sensitivity of 82.0% and specificity of 97.0%. Combination of CNN and LSTM was also used by Liang et al. [14], who verified the classification accuracy on three different datasets of raw ECG signals and obtained F1-scores of 85.0%, 80% and 82.6%. For detection of shockable rhythms in the presence and absence of cardiopulmonary resuscitation (CPR) artifact, Hajeb-M et al. applied deep-learning algorithm using convolutional layers, residual networks and BiLSTM [5]. The sensitivity, specificity, accuracy and F1-score were 95.2%, 86.0%, 88.1% and 83.5%, respectively.

IV. CONCLUSION

Automatic detection of artifacts in ECG signal is important goal in wearable monitoring systems in order to accurate determine subject's physical state. This work proposes to use deep learning technique for classifying ECG signal. LSTM network was used on a raw ECG signal that was divided into 10-s segments. The classification accuracy of 90.1% indicate that the proposed model shows promising results. The future work will include more data to improve the training of the neural network. Also, ECG signals with various degrees of noise will be considered. One of the possible applications of this research could be within the SIXTHSENSE project, to improve the existing algorithm for determining the heart rate signal from the ECG of the first responders (mountain rescuers and firefighters).

ACKNOWLEDGMENT

The authors would like to acknowledge that this research was supported by the Ministry of Education, Science and Technological Development of the Republic of Serbia (contract 451-03-68/2022-14/200103).

The work in this study was also performed within the SIXTHSENSE project, which has received funding by European Union's Horizon 2020 research and innovation programme under grant agreement No 883315.

REFERENCES

[1] Liu, C., Zhang, X., Zhao, L., Liu, F., Chen, X., Yao, Y., & Li, J. (2018). Signal quality assessment and lightweight QRS detection for wearable ECG SmartVest system. *IEEE Internet of Things Journal*, *6*(2), 1363-1374.

[2] Saadatnejad, S., Oveisi, M., & Hashemi, M. (2019). LSTM-based ECG classification for continuous monitoring on personal wearable devices. *IEEE journal of biomedical and health informatics*, *24*(2), 515-523.

[3] Yildirim, Ö. (2018). A novel wavelet sequence based on deep bidirectional LSTM network model for ECG signal classification. *Computers in biology and medicine*, *96*, 189-202.

[4] Chen, Y. J., Liu, C. L., Tseng, V. S., Hu, Y. F., & Chen, S. A. (2019, May). Large-scale classification of 12-lead ECG with deep learning. In *2019 IEEE EMBS International Conference on Biomedical & Health Informatics (BHI)* (pp. 1-4). IEEE.

[5] Hajeb-M, S., Cascella, A., Valentine, M., & Chon, K. H. (2021). Deep Neural Network Approach for Continuous ECG-Based Automated External Defibrillator Shock Advisory System During Cardiopulmonary Resuscitation. *Journal of the American Heart Association*, *10*(6), e019065.

[6] Chauhan, S., & Vig, L. (2015, October). Anomaly detection in ECG time signals via deep long short-term memory networks. In *2015 IEEE International Conference on Data Science and Advanced Analytics (DSAA)* (pp. 1-7). IEEE.

[7] Attia, Z. I., Kapa, S., Lopez-Jimenez, F., McKie, P. M., Ladewig, D. J., Satam, G., ... & Friedman, P. A. (2019). Screening for cardiac contractile dysfunction using an artificial intelligence–enabled electrocardiogram. *Nature medicine*, *25*(1), 70-74.

[8] https://sixthsenseproject.eu/

[9] Kłosowski, G., Rymarczyk, T., Wójcik, D., Skowron, S., Cieplak, T., & Adamkiewicz, P. (2020). The use of time-frequency moments as inputs of lstm network for ecg signal classification. *Electronics*, *9*(9), 1452.

[10] Goodfellow, I., Bengio, Y., & Courville, A. (2016). *Deep learning*. MIT press.

[11] Patterson, J., & Gibson, A. (2017). *Deep learning: A practitioner's approach*. " O'Reilly Media, Inc.".

[12] Gao, J., Zhang, H., Lu, P., & Wang, Z. (2019). An effective LSTM recurrent network to detect arrhythmia on imbalanced ECG dataset. *Journal of healthcare engineering*, *2019*.

[13] Kim, B. H., & Pyun, J. Y. (2020). ECG identification for personal authentication using LSTM-based deep recurrent neural networks. *Sensors*, *20*(11), 3069.

[14] Liang, Y., Yin, S., Tang, Q., Zheng, Z., Elgendi, M., & Chen, Z. (2020). Deep learning algorithm classifies heartbeat events based on electrocardiogram signals. *Frontiers in Physiology*, 1255.

 ISBN 978-86-7466-930-3

Inhibition Potency of Terpyridine Metal Complexes toward Penicillin-Binding Protein 1A

Svetlana Jeremić, Enisa Selimović, Milan Dekić, and Tanja Soldatović

***Abstract*—The potency of copper(II) and zinc(II) terpyridine complexes to inhibit penicillin-binding protein 1A (PBP1a) was investigated by *in silico* methods. The geometries of ligands are optimized using DFT calculations. In order to estimate the binding sites, inhibition constants and binding energies between ligands and PBP1a protein, molecular docking analysis is performed. The inhibition potency of examined terpyridine metal complexes is compared with the inhibition potency of lactivicin, an antibiotic already used in the treatment of Gram-negative and Gram-positive bacteria. Performed docking analysis indicated that investigated terpyridine metal complexes show higher inhibition potency toward PBP1a protein than lactivicin. The results identified these complexes as potential antimicrobial agents for further *in vitro* experiments.**

***Key words* — copper(II) terpyridine; zinc(II) terpyridine; penicillin-binding protein 1A; lactivicin; molecular docking analysis.**

I. Introduction

Antibiotics have transformed medicine by changing the outcome of bacterial infections. Since the discovery of penicillin by Sir Alexander Fleming in 1928, antibiotics extend expected life spans for almost 25 years in the USA and have had similar beneficial effects worldwide. Nevertheless, the emergence of resistant microorganisms endangering the efficacy of antibiotics - bacterial infections have again become a threat due to the resistance that has been seen to nearly all antibiotics that have been developed. This has been attributed to the overuse and misuse of antibiotics, as well as a lack of new drug development, urging to renew efforts in the research of new antimicrobials and investigation of their mechanism of action [1].

Epidemic antibiotic resistance has been described in numerous pathogens, including common respiratory pathogens such as *Streptococcus pneumoniae*. This pathogen causes pneumonia, otitis media, and sepsis, and has been responsible for over one million yearly deaths worldwide [2]. Presently, 25% of all invasive strains are resistant to penicillin, amoxicillin, and cephalosporins [3, 4].

Svetlana Jeremić is with the Department of Natural Sciences and Mathemathics, The State University of Novi Pazar, 9 Vuka Karadžića, 36300 Novi Pazar, Serbia (e-mail: sjeremic@np.ac.rs).

Enisa Selimović is with the Department of Natural Sciences and Mathemathics, The State University of Novi Pazar, 9 Vuka Karadžića, 36300 Novi Pazar, Serbia (e-mail: eselimovic@np.ac.rs).

Milan Dekić is with the Department of Natural Sciences and Mathemathics, The State University of Novi Pazar, 9 Vuka Karadžića, 36300 Novi Pazar, Serbia (e-mail: mdekic@np.ac.rs).

Tanja Soldatović is with the Department of Natural Sciences and Mathemathics, The State University of Novi Pazar, 9 Vuka Karadžića, 36300 Novi Pazar, Serbia (e-mail: tsoldatovic@np.ac.rs).

In the last few decades we have seen a dramatic increase in the number of β-lactam antibiotics and understanding of their mechanism in inhibition of peptidoglycan biosynthesis. Peptidoglycan component of bacterial cell wall consists of polymerized chains of repeating disaccharide subunits (N-acetylglucosamine and N-acetylmuramic acid cross-linked by stem pentapeptides), whose function is to provide cellular shape and maintain osmotic pressure [5]. Both the polymerization of disaccharide subunits and peptide cross-linking reactions are catalyzed by penicillin-binding proteins (PBPs), membrane-associated enzymes essential for cell division and daughter cell formation. PBPs possess the ability to covalently bind β-lactam antibiotics [6]. All enterobacteria appear to possess a similar spectrum of PBPs differing in molecular weight and affinity for β-lactams [7]. The high molecular-weight (HMW) PBPs (PBP1a/1b, PBP2, and PBP3) are physiologically important bifunctional enzymes that catalyze the final stages of peptidoglycan synthesis [6].

In Gram-positive bacteria, such as *S. pneumoniae*, the cell wall is composed mostly of peptidoglycan. *S. pneumoniae* has six PBPs, three of which are bifunctional - PBP1a, PBP2a, and PBP1b [8]. A PBP1a is essential for cell viability. This protein plays a key role in the formation of the cell septum during the bacterial division cycle and is involved in homologous DNA recombination mechanism, repair, and chromosome segregation [2]. To date, the mechanism used by bifunctional PBPs in the development of β-lactam resistance has remained unknown [2]. X-ray studies of soluble forms of pneumococcal PBP1a, both in apo (an inactive form, with no bounded ligand) as well as in antibiotic-bound forms, demonstrate that this protein contains three domains – the central transpeptidase domain flanked N-terminally by a GT/TP interdomain linker region, and C-terminally by a small, β-sheet rich unit. The active site of PBP1a is unusually narrow, suggesting that ligands must initially be threaded into the gorge to be recognized [2].

The search for effective inhibitors of PBP1a protein indicated that among the molecules with significant inhibitory affect there are different metal complexes of 2,2′:6′,2′′-terpyridine molecule. The 2,2′:6′,2′′-terpyridine (terpy) ligand is tridentate, nearly coplanar, N_3 donor ligand. It has been recognized as a useful ligand for transition metal and rare earth metal ions in inorganic chemistry. Square-planar, square-pyramidal and octahedral metal complexes with terpy ligands have been reported to be of great biological interest [9, 10, 11].

The biologically important metal ions copper(II) and zinc(II) have the ability to coordinate into different

 ISBN 978-86-7466-930-3

geometries depending on the specific arrangement of donor atoms in biomolecules, but strong π-acceptor ability of the tridentate chelate 2,2′:6′,2′′-terpyridine stabilizes the square-pyramidal geometry [10]. Different substituted terpyridene molecules generate complexes with copper(II) and zinc(II) ions, that exert anti-microbial, anti-bacterial, anti-fungal, anti-proliferative and inhibitory activity. For example, terpyridine complexes of Cu(II) and Zn(II), and especially complexes of Cu(TTP)Cl_2 and Zn(TTP)Cl_2 (TTP is 4 -[*p*-tolyl]- 2,2′:6′,2′′-terpyridine) are efficient inhibitors of furin. Furin, a human subtilisin-related proprotein convertase (SPC), is emerging as an important pharmaceutical target because it processes vital proteins of many aggressive pathogens. Inhibition is irreversible, competitive with substrate, and affected by substituents on the chelate. The free chelates are not inhibitors [12]. Complexes of terpyridine-based ligands with Zn(II) as a central metal ion has also shown significant inhibitory activity against B-DNA molecule and similar double helixes, as against penicillin binding protein 2a [9]. This fact indicated the importance of examining the possibility of complexes of terpyridine with Cu(II) and Zn(II) to inhibit PBPa1 protein, which is known to be a protein of great importance in the development of bacteriological infections.

II. Methodology Section

The inhibition potency of copper(II) and zinc(II) terpyridine complexes toward penicillin-binding protein 1A (PBP1a) is investigated using molecular docking analysis. The structures of terpyridine metal complexes are optimized using M06-2X functional [13] in combination with 6-311++G(d,p) basis set implemented in Gaussian 09 program package [14]. Molecular docking simulations were carried out using AutoDock 4.0 software [15]. The three-dimensional (3D) crystal structure of PBP1a protein was downloaded from the Protein Data Bank (PDB ID: 2C6W) [2]. The protein structure is released from the co-crystallized ligand, water molecules, and co-factors and prepared for docking simulations using Discovery Studio 4.0 [16]. The affinity maps of the target protein are established using AGFR (AutoGridFR) software [17]. According to AGFR, binding site with the lowest expected binding energy is grid box with dimensions 98.799Å x 35.214Å x 55.068Å in -x, -y, and -z directions. A grid point spacing of 0.375 Å was used for auto grid runs. The addition of polar hydrogen atoms and the calculation of Kollman charges are done by using AutoDockTools (ADT) graphical interface. The ligands are set to be flexible, while the structure of protein remains standing as rigid. The Lamarckian Genetic Algorithm (LGA) is used for protein-ligand flexible molecular docking simulations. Calculations are performed at a temperature of 298.15 K. Analysis of molecular docking simulation results and visualizations of predicted protein-ligand interactions are performed using BIOVIA Discovery Studio [16].

III. Results and Discussions

Molecular docking analysis is a useful and widely used method for predicting the inhibitory activity of biologically active compounds. Terpyridine metal complexes possess significant anti-bacterial, anti-fungal and anti-cancerous activity [9, 10]. Moreover, recent research has shown that complexes of terpyridine and some its derivatives with different metals show significant inhibitory activity against various protein molecules [18, 19]. Since terpyridine complexes of Cu(II) and Zn(II) are already selected as potential agents against different disease, here is investigated their potency to inhibit PBP1a protein. PBP1a protein is membrane-associated enzyme that plays essential roles in the peptidoglycan biosynthetic process [2]. In this way it enables the proliferation of bacteria *Streptococcus pneumoniae*. The infection caused by this pathogen have been treated with β-lactam antibiotics for almost a century, but the proliferation of strains that are highly resistant to such drugs is a problem of worldwide concern. Although *S. pneumoniae* has six penicillin-binding proteins, PBP1a is essential for the development of high-level resistance to penicillins and cephalosporins [2]. Therefore, the development of agents that enable the inhibition of this protein is of particular interest.

In order to be able to compare the inhibitory activity of terpyridine metal complexes with an activity of a compound already used for these purposes, the inhibitory potency of the drug lactivicin was also examined. Lactivicin is compound that shows moderate activity against Gram-negative and high activity against Gram-positive bacteria. The mechanism of its activity is based on the binding to PBPs and violation of its structure [20]. Structures of copper(II) terpyridine complex, zinc(II) terpyridine complex and lactivicin are shown in Fig. 1.

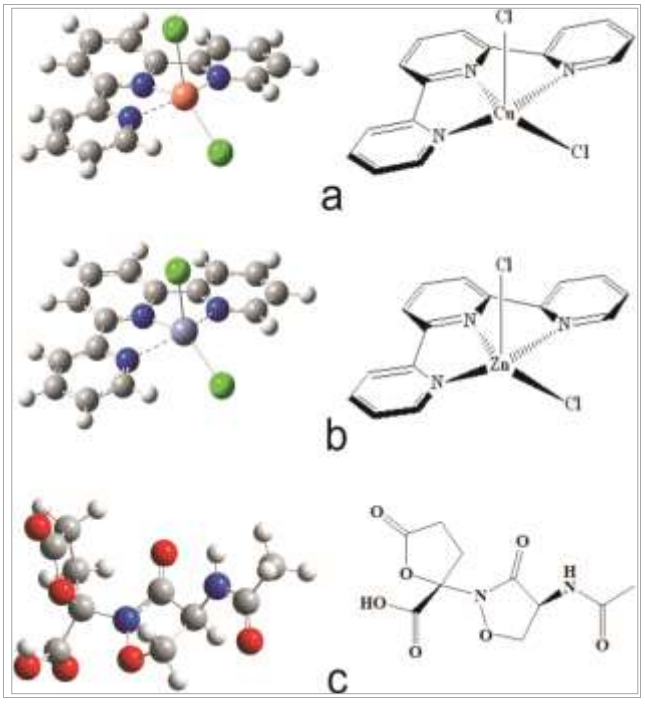

Fig. 1. 2D structures (right) and optimized structures (left) of copper(II) terpyridine complex (a), zinc(II) terpyridine complex (b) and lactivicin (c).

The evaluation of the inhibitory nature of ligand according to PBP1a was performed using molecular docking study. At the beginning of the research, the pockets and binding sites of the targeted protein were determined using the AGFR software [17]. All three estimated ligands showed

 ISBN 978-86-7466-930-3

the highest activity against protein at the same position. Grid box with dimensions 98.799Å x 35.214Å x 55.068Å in -x, -y, and -z directions, and with spacing of 0.375 Å is predicted. For all three estimated ligands it comprises the same pocket of the polypeptide chain (Fig.2).

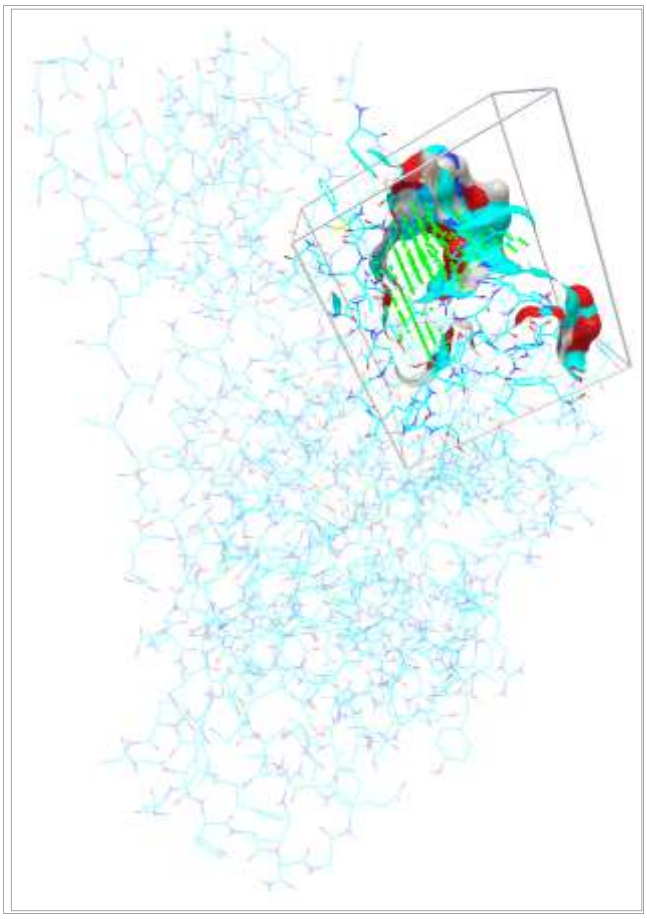

Fig. 2. The location of the most probable binding site of PBP1a for all three estimated ligands.

After configuring and computing affinity maps for a receptor-protein interactions, the one with the lowest binding energy was used for AutoDock4 calculations. Ten different conformations of protein-ligand complexes are set for molecular docking simulations. It should be emphasized that only one conformation has been accomplished when as ligand is used any of estimated terpyridine metal complexes. It can be explained by the complete rigidity of the ligand structure. On the other side, flexible structure of lactivicin allowed formation of ten protein-ligand complexes. The complex conformation that possesses the lowest binding energy was selected for further analysis.

TABLE I

THE IMPORTANT THERMODYNAMICAL PARAMETERS FROM MOLECULAR DOCKING SIMULATIONS BETWEEN PENICILLIN-BINDING PROTEIN 1A (PBP1A) (PDB ID: 2C6W) AND SELECTED COMPOUNDS

Ligand	ΔG_{bind} (kcal/mol)	Ki (μM)
$[CuCl_2(terpy)]$	-6.66	13.11
$[ZnCl_2(terpy)]$	-6.62	13.99
lactivicin	-5.48	95.46

The inhibitory potency of preferred compounds can be estimated based on the thermodynamical parameters obtained by statistical mechanical analysis. Values of the free energy of binding (ΔG_{bind}) expressed in kcal/mol and inhibition constant (Ki) expressed as micromolar concentration, are presented in Table 1. The lowest binding energy indicates to the easiest binding possibility of the investigated ligand. Low values of the inhibition constant indicate that a low concentration of inhibitor is required in order to inhibit the activity of the observed protein. Both ΔG_{bind} and Ki indicate that the highest inhibition potency shows Cu(II)-terpyridine complex. Somewhat lower inhibition potency has Zn(II)-terpyridine complex, while lactivicin shows the least.

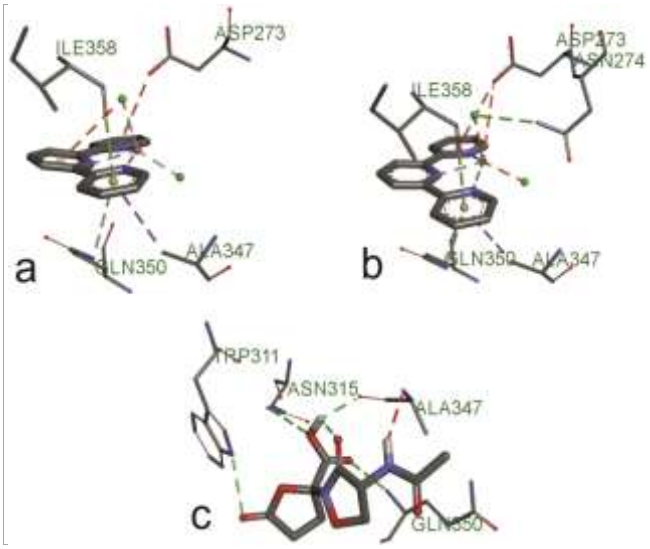

Fig. 3. Docking positions of the Cu(II)-terpyridine complex (a), Zn(II)-terpyridine complex (b) and lactivicin (c), with PBP1a protein.

Each of the three considered ligands achieves at least four protein-ligand interactions. PBP1a protein interact with Cu(II)-terpyridine complex forming π – anion electrostatic interaction via Asp273, then π – lone pair interaction via Ile358, π – donor hydrogen bond via Gln350, and π – σ interaction via Ala347. The interactions achieved by Zn(II)-terpyridine complex with PBP1a are the same as those achieved by the complex with copper, except that Zn-complex achieves another additional conventional hydrogen bond via Asn274 amino acid of PBP1a. Lactivicin generates with the protein four conventional hydrogen bonds, via the amino acids Trp311, Asn315, Ala347 and Gln350. It can be seen that all three ligands interact with PBP1a via Ala347 and Gln350 (Fig. 3). As it can be concluded, the number of ligand-protein interactions is not the only parameter that affects to the strength of inhibition, but it is also the type of interactions. Although conventional hydrogen bonds are among the most significant interactions in protein inhibition, the effect of interactions involving π–electrons derived from terpyridine should not be overlooked.

IV. CONCLUSIONS

Metal complexes of terpyridine are known as compounds with significant anti-bacterial, anti-fungal and anti-

 ISBN 978-86-7466-930-3

cancerous activity [9, 10]. On the other hand, there are numerous infections caused by bacteria *Streptococcus pneumonia*. Penicillin binding proteins (PBPs) play a key role in the proliferation of this bacterium [2]. Therefore, the device of molecules that would lead to the inhibition of this protein could significantly contribute to the treatment of infections caused by *S. pneumonia*.

The potency of Cu(II)-terpyridine complex and Zn(II)-terpyridine complex to inhibit penicillin-binding protein 1A (PBP1a) is investigated in this purpose. Due to it molecular docking simulations are performed. Inhibition potency of $[CuCl_2(terpy)]$ and $[ZnCl_2(terpy)]$ are compared with inhibition potency of lactivicin, molecule that is already used in the treatment of *S. pneumonia*.

The analysis of results obtained by molecular docking simulations indicated that the highest inhibition potency express Cu(II)-terpyridine complex, while Zn(II)-terpyridine complex shows somewhat lower inhibition potency. Both estimated complexes possess higher inhibition potency than lactivicin. All three investigated ligands react with PBP1a at the same reaction position, and in some cases, via the same amino acids of protein. All ligands generate at least four interactions with protein, among the most important are conventional hydrogen bonds, and interactions involving π–electrons from terpyridine.

Comparing inhibition potency of $[CuCl_2(terpy)]$ and $[ZnCl_2(terpy)]$ with inhibition potency of some other complexes of terpyridine and its derivatives with different metals [18, 19], it can be seen that here investigated complexes possess similar or higher inhibition potency toward here estimated protein.

The results of the docking analysis conducted in this study provide significant preliminary results related to the inhibitory activity of the complexes tested here. With all this in mind, the herein discussed metal complexes may be considered as potential agents in the treatment of bacterial infections. Among further studies of the biological activity of the terpyridine complex, *in vivo* studies are certainly the most important.

ACKNOWLEDGMENT

This research was supported by the Serbian Ministry of Education, Science, and Technological Development (Agreement No. 451-03-68/2022-14/200252).

REFERENCES

[1] C. L. Ventola C. L., "The antibiotic resistance crisis: part 1: causes and threats," *P T.*, vol. *40*, no. *4*, pp. *277-283*, Apr. 2015.

[2] C. Contreras-Martel, V. Job, A. M. Di Guilmi, T. Vernet, O. Dideberg, A. Dessen, "Crystal structure of penicillin-binding protein 1a (PBP1a) reveals a mutational hotspot implicated in beta-lactam resistance in Streptococcus pneumoniae," *J. Mol. Biol.*, vol. *355*, no. *4*, pp. *684-696*, Nov. 2005.

[3] C. Doit, C. Loukil, F. Fitoussi, P. Geslin, E. Bingen, "Emergence in France of multiple clones of clinical Streptococcus pneumoniae isolates with high level resistance to amoxicillin," *Antimicrob. Agents Chemother.* vol .*43*, no. *6*, pp. *1480-1483*, Jun 1999.

[4] T. J. Coffey, M. Daniels, L. K. McDougal, C. G. Dowson, F. C. Tenover, B. G. Spratt, "Genetic analysis of clinical isolates of Streptococcus pneumoniae with high-level resistance to expanded-spectrum cephalosporins," *Antimicrob. Agents Chemother.*, vol. *39*, no. *6*, pp. *1306-1313*, Jun 1995.

[5] J. V. Holtje, "Growth of the stress-bearing and shape-maintaining murein sacculus of *Escherichia coli*," *Microbiol. Mol. Biol. Rev.*, vol. *62*, no. *1*, pp. *181-203*, Mar. 1998.

[6] R. Fontana, G. Cornaglia, M. Ligozzi, A. Mazzariol, "The final goal: penicillin-binding proteins and the target of cephalosporins," *Clin. Microbiol. Infect.*, vol. *6*, no. *3*, pp. *34-40*, Jan. 2000.

[7] N. A. Curtis, D. Orr, G. W. Ross, M. G. Boultan, "Competition of beta-lactam antibiotics for the penicillin-binding proteins of *Pseudomonas aerogenes, Proteus rettgeri, and Escherichia coli*. Companion with antibacterial activity and effects upon bacterial morphology," *Antimicrob. Agents. Chemother.*, vol. *16*, no. *3*, pp. *325-328*, Sep. 1979.

[8] C. Goffin, J. M. Ghuysen, "Multimodular penicillin-binding proteins: an enigmatic family of orthologs and paralogs," *Microbiol. Mol. Biol. Rev.*, vol. *62*, no. *4*, pp. *1079-1093*, Dec. 1998.

[9] E. U. Mughal, M. Mirzaei, A. Sadiq, S. Fatima, A. Naseem, N. Naeem, N. Fatima, S. Kausar, A. Ali Altaf, M. N. Zafar, B. A. Khan, "Terpyridine-metal complexes: effects of different substituents on their physico-chemical properties and density functional theory studies," *R. Soc. Open Sci.*, vol. *7*, no. *11*, pp. e*201208*, Nov. 2020.

[10] E. Selimović, S. Jeremić, B. Ličina, T. Soldatović, "Kinetics, DFT study and antibacterial activity of zinc(II) and copper(II) terpyridine complexes," *J. Mex. Chem. Soc.*, vol. 62, no. *1*, pp. *1-18*, Mar. 2018.

[11] J. Li, R. Liu, J. Jiang, X. Liang, L. Huang, G. Huang, H. Chen, L.Pan, Z. Ma, "Zinc(II) Terpyridine Complexes: Substituent Effect on Photoluminescence, Antiproliferative Activity, and DNA Interaction," *Molecules.*, vol. *24*, no. *24*, pp. *4519-4546*, Dec. 2019.

[12] P. Podsiadlo, T. Komiyama, R. S. Fuller, O. Blum, "Furin inhibition by compounds of copper and zinc," *J. Biolog. Inorg. Chem.*, vol. 279, no. 35, pp. 36219-36227, Aug. 2004.

[13] Y. Zhao, D. G. Truhlar, "The M06 suite of density functionals for main group thermochemistry, thermochemical kinetics, noncovalent interactions, excited states, and transition elements: two new functionals and systematic testing of four M06- class functionals and 12 other functionals," *Theor. Chem Acc.*, vol. *120*, no. *1-3*, pp. *215-241*, Jan. 2008.

[14] M. J. Frisch, G. W. Trucks, H. B. Schlegel, G. E. Scuseria, M. A. Robb, J. R. Cheeseman, G. Scalmani, V. Barone, G. A. Petersson, H. Nakatsuji, X. Li, M. Caricato, A. Marenich, J. Bloino, B. G. Janesko, R. Gomperts, B. Mennucci, H. P. Hratchian, J. V. Ortiz, A. F. Izmaylov, J. L. Sonnenberg, D. Williams-Young, F. Ding, F. Lipparini, F. Egidi, J. Goings, B. Peng, A. Petrone, T. Henderson, D. Ranasinghe, V. G. Zakrzewski, J. Gao, N. Rega, G. Zheng, W. Liang, M. Hada, M. Ehara, K. Toyota, R. Fukuda, J. Hasegawa, M. Ishida, T. Nakajima, Y. Honda, O. Kitao, H. Nakai, T. Vreven, K. Throssell, J. A. Montgomery, Jr., J. E. Peralta, F. Ogliaro, M. Bearpark, J. J. Heyd, E. Brothers, K. N. Kudin, V. N. Staroverov, T. Keith, R. Kobayashi, J. Normand, K. Raghavachari, A. Rendell, J. C. Burant, S. S. Iyengar, J. Tomasi, M. Cossi, J. M. Millam, M. Klene, C. Adamo, R. Cammi, J. W. Ochterski, R. L. Martin, K. Morokuma, O. Farkas, J. B. Foresman, D. J. Fox, Gaussian 09, Revision A.02, Gaussian, Inc., Wallingford CT, 2016.

[15] G. M. Morris, R. Huey, W. Lindstrom, M. F. Sanner, R. K. Belew, D. S. Goodsell, A. J. Olson, "AutoDock4 and AutoDockTools4: Automated docking with selective receptor flexibility," *J. Comput. Chem.*, vol. *30*, no. *16*, pp. *2785-2791*, Dec. 2009.

[16] D. S. Biovia, Discovery studio modeling environment, 2017.

[17] Y. Zhang, S. Forli, A. Omelchenko, M. F. Sanner, "AutoGridFR: improvements on AutoDock affinity maps and associated software tools," *J. Comput. Chem.*, vol. *40*, no. *32*, pp. *2882-2886*, Dec. 2019.

[18] E. U. Mughal, M. Mirzaei, A. Sadiq, S. Fatima, A. Naseem, N. Naeem, N. Fatima, S. Kausar, A. Ali Altaf, M. N. Zafar, B. A. Khan, "Terpyridine-metal complexes: effect of different substituents on their physic-chemical properties and density functional theory studies," *Roy. Soc. Open Sci.*, vol. *7*, no. *11*, *e201208*, May 2022.

[19] X. Liang, J. Jiang, X. Xue, L. Huang, X. Ding, D. Nong, H. Chen, L. Pan, Z. Ma, "Synthesis, characterization, photoluminescence, anti-tumor activity, DFT calculations and molecular docking with proteins of zinc(II) halogen substituted terpyridine compounds," *Dalton Trans.*, vol. *48*, pp. *10488-10504*, Dec. 2019.

[20] Y. Nozaki, N. Katayama, S. Harada, H. Ono, H. Okazaki, "Lactivicin, a naturally occurring non-beta-lactam antibiotic having beta-lactam-like action: biological activities and mode of action," *J. Antibiot.*, vol. 4*2*, no. *1*, pp. *84-93*, Jan. 1989.

 ISBN 978-86-7466-930-3

GT Analyzer – A Basic Tool for Handwriting Movement Data

Vladimir Džepina, Nikola Ivančević, Vera Miler-Jerković, Blažo Nikolić, Dejan Stevanović, Jasna Jančić and Milica M. Janković, *Member*, IEEE

***Abstract*—In the presence of neurological and psychiatric diseases, sensorimotor and cognitive skills tend to deteriorate. One of the daily activities that could be easily affected is handwriting. In this paper, we present the open-source software GT Analyzer, developed for visual analysis and feature extraction of the handwriting data acquired by graphic tablet. Data is acquired while patients are working on graphic tasks developed by clinicians. Visual and feature analysis of handwriting data could be of great use in establishing a correct diagnosis or in following the changes during medical therapies for neurological and psychiatric diseases. Furthermore, extracted features can be used later in statistical tools, to improve the classification and determination of therapeutic effects to a greater extent.**

***Index Terms*—handwriting; graphic tablet; depression; Parkinson's disease; open-source**

I. Introduction

Handwriting is a complex motor task consisting of both cognitive and motor processes interplaying together [1, 2]. Computer analysis of handwriting, using a digital writing tablet, has shown its usefulness in clinical studies in the fields of neurology, psychiatry and neuropsychology in both adults and children [3]. Data obtained from handwriting analysis could help clinicians to establish correct diagnosis e.g. in Parkinson's disease and Parkinsonism [4-6], or to track changes in motor functioning and the influence of therapy on it in depression in adult subjects [7] or in attention deficit hyperactivity disorder/ADHD in children [8].

The summary of computer analysis of handwriting is that clinicians are giving patients several specially designed drawing and/or writing tasks, which they have to draw or write on a graphic tablet [2, 3, 4, 6]. During the task, the tablet is acquiring the position of the pen and the pressure with which the pen is pressed on the tablet [2]. Both on-surface and in-air handwriting movements can be analyzed [6]. After the task is completed, acquired data can be operationalized through kinematic handwriting features [2, 4].

This system is favored as it has low complexity of installment, has great ease of use for both patients and clinicians and has low chances of errors while performing the task. Also, kinematic handwriting features acquired using writing tablets show high test-retest reliability [2].

Our previous research [3, 6, 8-10] in the field of handwriting analysis has shown a great need for an open-source, user-friendly software suitable for data acquisition alongside the application software that will be used for later exploration of acquired data. This could help make the research methodology more uniform and to ease data exchange and comparison between different studies.

The aim of this paper is to present a novel, user-friendly, open-source interface for reading, visualization and analysis of data that was acquired during different graphic tasks on digital graphic tablets. This software also stresses out the importance of visual analysis of extracted handwriting features.

The flowchart of the implemented interface and software options are presented in Section II. The software functionality is demonstrated through examples from two different datasets in Section III. A brief overview of software advantages and usage options is presented in the Conclusion section.

II. The Method

Graphic Task Analyzer (GT Analyzer) is an open-source application that enables the reading of recorded pen position (X,Y) and pen pressure (p) data from digital graphic tablets, a simple preview of calculated kinematic features of handwriting over time and export of 173 standard kinematic handwriting features, Fig. 1. An example of visualization for (X,Y,p) input sequence for three drawn figures (figure separators are marked by green arrows) is also presented in Fig. 1.

Vladimir Džepina is with the School of Electrical Engineering, University of Belgrade, Bulevar kralja Aleksandra 73, 11020 Belgrade, Serbia (e-mail: dzepina.vladimir@gmail.com).

Nikola Ivančević is with the Clinic of Neurology and Psychiatry for Children and Youth, Faculty of Medicine, University of Belgrade, Serbia (email: ivancevicsd@gmail.com).

Vera Miler-Jerković is with the Innovation Center, School of Electrical Engineering, University of Belgrade, Bulevar kralja Aleksandra 73, 11120 Belgrade, Serbia (e-mail: vera.miler@etf.bg.ac.rs).

Blažo Nikolić is with the Clinic of Neurology and Psychiatry for Children and Youth, Faculty of Medicine, University of Belgrade, Serbia (e-mail: blazonikolic87@gmail.com).

Dejan Stevanović is with the Clinic of Neurology and Psychiatry for Children and Youth, Faculty of Medicine, University of Belgrade, Serbia, Gillberg Neuropsychiatry Centre, Institute of Neuroscience and Physiology, Sahlgrenska Academy, University of Gothenburg, Sweden (email: stevanovic.dejan79@gmail.com).

Jasna Jančić is with the Clinic of Neurology and Psychiatry for Children and Youth, Faculty of Medicine, University of Belgrade, Serbia (e-mail: jasna.jancic.npk@gmail.com).

Milica M. Janković is with the School of Electrical Engineering, University of Belgrade, Bulevar kralja Aleksandra 73, 11020 Belgrade, Serbia (e-mail: piperski@etf.bg.ac.rs).

 ISBN 978-86-7466-930-3

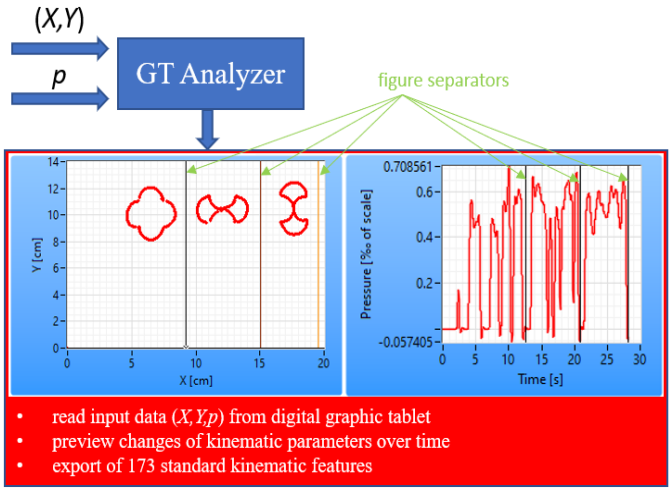

Fig. 1. GT Analyzer software options with preview example of input data (coordinate pair (*X,Y*) and pressure *p* of the pen tip)

A. *Software description*

The application was developed in the LabVIEW 2019 environment (National Instruments, Texas, USA). The code of the software is available at the following Github link: https://github.com/MagnumSinum/GT-Analyzer/blob/main/GT%20Analyzer%20source%20code.rar

B. *Kinematic features*

For each (*X,Y,p*) input sequence, the algorithm calculates the 1st, 2nd and 3rd derivatives. The 1st derivatives of *X(t)* data and *Y(t)* data correspond to the velocity $V_x(t)$ and $V_y(t)$, respectively. The total velocity $V = \sqrt{V_x^2 + V_y^2}$ was also calculated. The 1st derivative of *p(t)* data corresponds to $dp(t)/dt$. The 2nd derivatives of *X(t)* data and *Y(t)* data correspond to the acceleration $A_x(t)$ and $A_y(t)$, respectively. The total acceleration *A(t)* corresponds to the 1st derivative of *V(t)*. The 2nd derivative of *p(t)* data corresponds to $d^2p(t)/dt^2$. The 3rd derivatives of *X(t)* data and *Y(t)* data correspond to the jerk $J_x(t)$ and $J_y(t)$, respectively. The total jerk *J(t)* corresponds to the 2nd derivative of *V(t)*. The 3rd derivative of *p(t)* data corresponds to $d^3p(t)/dt^3$. The list of implemented statistical handwriting features is presented in Table 1.

TABLE I THE LIST OF STATISTICAL HANDWRITING FEATURES

Data	Statistical feature
X(t),Y(t),p(t), $V_x(t),V_y(t)$, *V(t),* $dp(t)/dt$, $A_x(t),A_y(t)$, *A(t),* $d^2p(t)/dt^2$, $J_x(t),J_y(t)$, *J(t),* $d^3p(t)/dt^3$	Median value
	Mean value
	Standard deviation
	Variance
	Coefficient of variation
	Maximum value
	Minimum value
	10th percentile
	25th percentile
	75th percentile
	90th percentile
Total variables =15	*Total number of features=11*

For each figure, 8 kinematic features, so-called "figure features" were calculated. The list of figure features is presented in Table 2.

TABLE II THE LIST OF FIGURE FEATURES

Abbreviation	Figure feature
FL [cm]	Figure length
FT [s]	Figure drawing time
FS [cm/s]	Figure drawing speed
NCV [n.u.]	Number of changes in velocity
RNCV [n.u.]	Number of changes in velocity relative to figure drawing time (NCV/FT)
NST [n.u.]	Time spent during drawing on-surface or in-air normalized by the figure drawing time (ON-SURFACE TIME/FT or IN-AIR TIME/FT)
NCA [n.u.]	Number of changes in acceleration
RNCA [s^{-1}]	Number of changes in acceleration relative to figure drawing time (NCA/FT)

C. *Implementation details*

The expected input file format for GT Analyzer tool is a textual file with 3 columns, each column corresponding to *X(t)*, *Y(t)* and *p(t)* data respectively, obtained by the data acquisition software from the digital graphic tablet. Expected units of the position data (*X,Y*) are meant to be 10^{-5} m. The pressure data *p(t)* is unitless because it is expected to be expressed relative to the full pressure scale of the digital graphic tablet. Also, it is expected that in the input file name first 4 characters are reserved for the subject ID and the last single digit in the file name is reserved for the number of the performed task by the subject. Each task could include up to eight figures.

Within the GT Analyzer tool, the following setting parameters could be selected:

- input file name (two file names could be selected at once in order to compare results for two subjects (e.g. patient vs. healthy data))
- input folder name (with several input files) for the automatic analysis and export of all kinematic features to one excel file per task.
- sample rate (performed by the data acquisition software used for (*X,Y,p*) data recording from the digital graphic tablet)
- lower cut-off frequency that will be performed in (*X,Y*) data processing by the 3rd order low pass Butterworth filter, the default value is set to 2 Hz
- NCV tolerance (minimal difference between two time-adjacent samples of *V(t)* to count it as a change in velocity, the default value is set to 0.1 cm/s)
- NCA tolerance (minimal difference between two time-adjacent samples of *A(t)* to count it as a change in acceleration, the default value is set to 1 cm/s^2)
- *Width* parameter (the number of consecutive data points to be used in the quadratic least-squares fit when the tool is determining local minimums on V_y – local minimums on V_y

 ISBN 978-86-7466-930-3

separate different strides within the figure)

- *Threshold* parameter (maximum value of local minimums that will be accepted when the tool is determining local minimums on V_y).

After the adjustment of parameters, the user can perform the following actions:

- DISPLAY DATA: Process (*X,Y,p*) input sequence from input files – extraction of all features defined in *Section II B Kinematic features*. Display (*X,Y*) data on XY graph, as well as a display of temporal graphics for $p(t)$, $V_y(t)$, $V(t)$, $A(t)$ and $J(t)$ from two selected input files. The software differentiates (*X,Y,p*) samples when the pen was on the surface or in-air and represents it with red and blue color, respectively. Stride ends (found local minimums on V_y) are presented by green circles on $V_y(t)$, $V(t)$, $A(t)$ and $J(t)$ graphics.
- SAVE LIMITS: Figure separators (separators between data for different figures in one task) could be set using cursors on XY graphs (up to eight) and the cursor limits could be saved for each task.
- EXPORT LOADED DATA: Extracted kinematic features could be saved in one .xls file per each selected input file.
- EXPORT FOLDER DATA: Extracted kinematic features could be saved in one .xls file for each file within the selected input folder.

All settings and actions can be repeated while the GT Analyzer application is still running.

D. Dataset description

Two different datasets acquired during graphic tablet tasks have been used to present the functionality of the GT Analyzer software:

- PaHaW adult subjects dataset, presented by Drotar and others [4] - labeled as DS1,
- pediatric subjects dataset used in the Doctoral dissertation of Ivančević N. D. [9] - labeled as DS2.

One pair from each dataset (one healthy and one diseased subject from DS1 and DS2, paired by gender and handedness), was selected to demonstrate the GT Analyzer interface. From DS1, the subject ID 6 (diagnosed with Parkinson's disease) and the healthy subject ID 26 were selected for the "drawing a spiral". During this task, the subject starts the drawing from the center of the spiral. From DS2, the subject ID 17, diagnosed with pediatric-onset major depressive disorder (drug-naive), and the healthy subject ID 25 were selected for the writing of two figures of the consecutive cursive letter "l": 1) figure 1 was drawn in the large rectangle 40x160 mm and 2) figure 2 was drawn in the small rectangle 9x160 mm.

Data acquisition for both DS1 (sample rate 100 Hz) and DS2 (sample rate 200 Hz) was performed using a digital graphic tablet Wacom Intous4 XL (Wacom Europe GmbH, Krefeld, Germany) with the cordless pen that enables on-surface and in-air handwriting. Custom-made data acquisition *LabHand* [10] previously developed in the LabVIEW environment, the same environment as for the GT Analyzer, was used for the data recording.

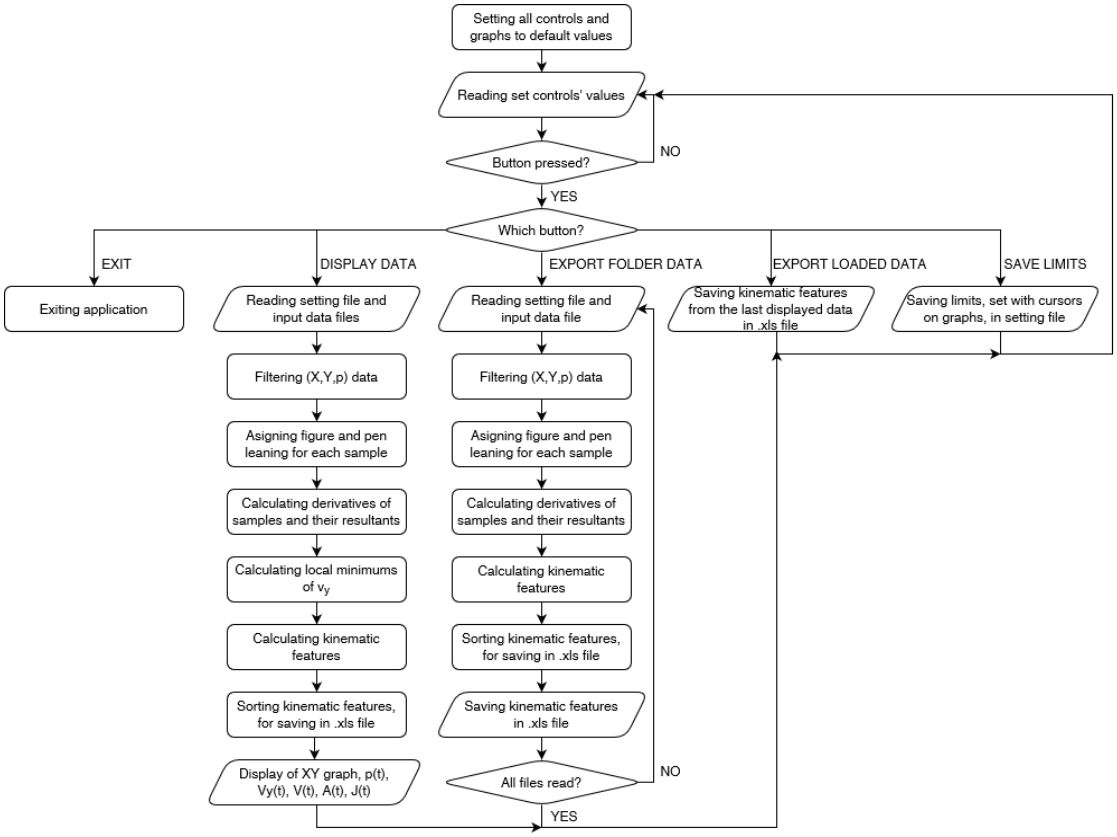

Fig. 2. GT Analyzer flowchart

 ISBN 978-86-7466-930-3

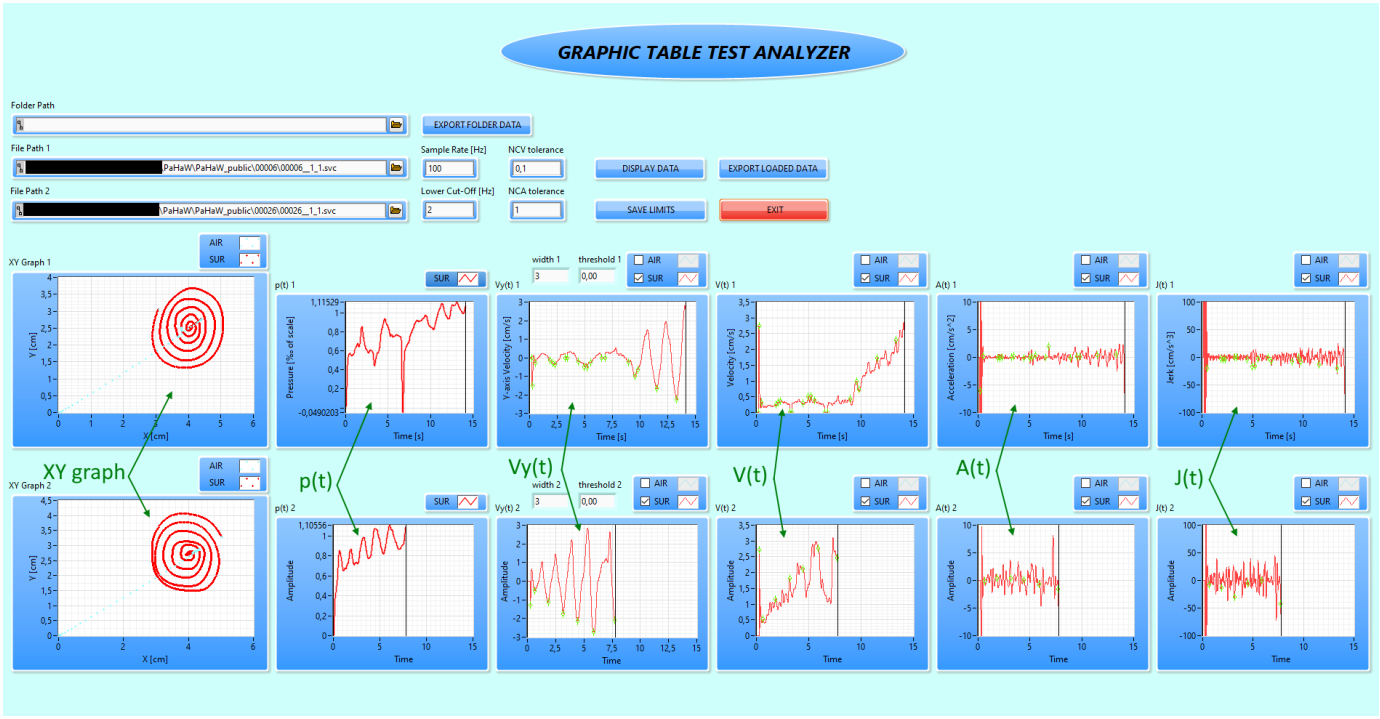

Fig. 3. An example of GT Analyzer interface from DS1 for "drawing a spiral" task (top graphics of subject ID 6 diagnosed with Parkinson's disease and bottom graphics of healthy subject ID 26)

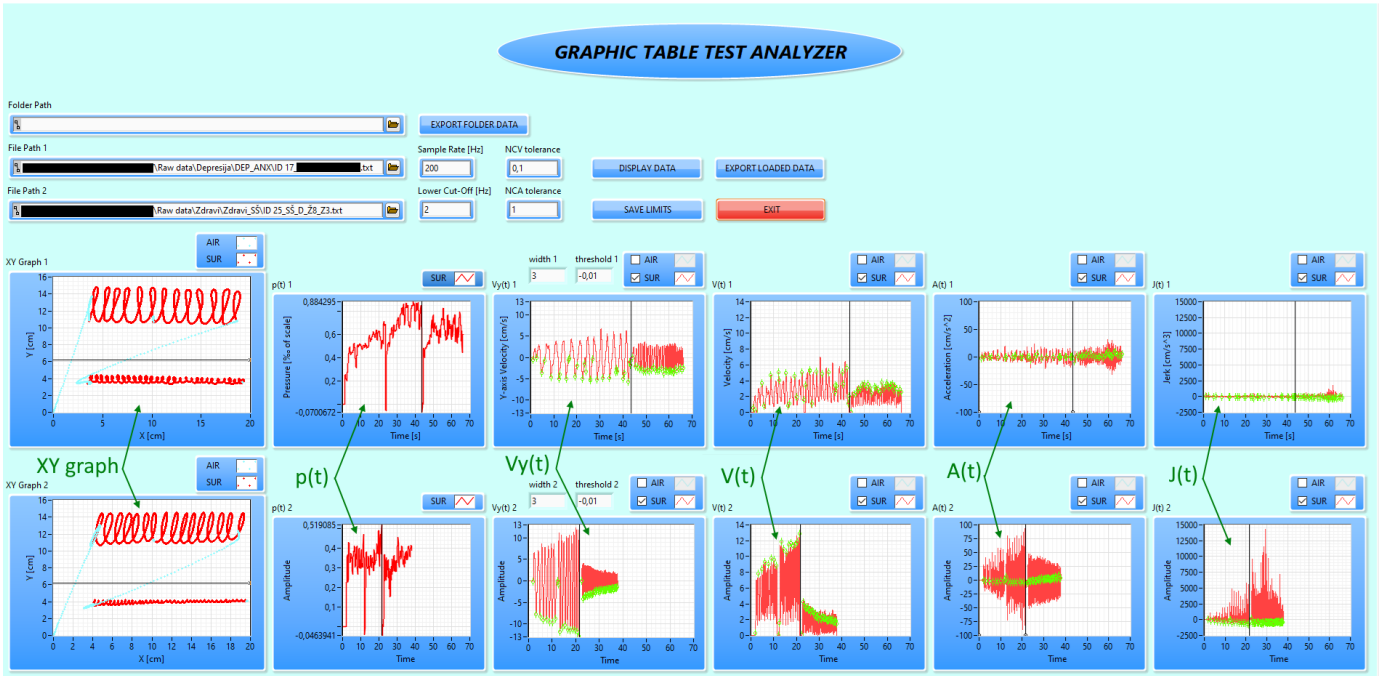

Fig. 4. An example of GT Analyzer interface from DS2 for writing two figures: the cursive letter "l" in 1) large rectangle and 2) small rectangle (top graphics of subject ID 17 diagnosed with major depressive disorder and bottom graphics of healthy subject ID 25)

III. Results

Two examples of the GT Analyzer interface after loading selected subjects from DS1 and DS2 (see *Section II D. Dataset description*) are presented in Fig. 3 and Fig. 4, respectively

In Fig. 3, it is evident that the subject with Parkinson's disease needs more time to finish a task and that he had trouble at the beginning of the task, where fine movements are hampered due to micrographia seen in Parkinson's disease This resulted in a significant increase in local minimums of V_y. Both facts are expected from patients with Parkinson's disease [11].

In Fig. 4, there is a similarity in pressure graphs for the patient with depression and the healthy subject. Both subjects

 ISBN 978-86-7466-930-3

took a break in a similar place while writing the first part of the task (cursive letter "l" in a large rectangle), which is represented as a pressure drop. That is also evident on the XY graph where the blue line presents in-air movement. One of the main kinematic descriptors of depression, psychomotor slowing/retardation, is more pronounced with larger scale movements. That is why a drop in speed amplitude and a significant increase in writing duration are evident in the subject with depression while writing the first part of the task [12].

IV. Conclusion

In this paper, a novel application for visual analysis of handwriting (drawing) tasks is presented. This user-friendly, open-source, clinically validated interface with implemented all standard kinematic features for handwriting analysis has the potential of helping users visually determine differences between healthy and diseased subjects. Furthermore, it can export the conventional kinematic features that can be used later in statistical analysis or classification procedures. The developed analysis software could be integrated with the previously developed data acquisition *LabHand* [10] software as a unique package for the overall handwriting data acquisition, analysis and kinematic feature extraction.

Future work will be focused on greater flexibility and compatibility of the application, as well as on defining and adding new features that will be used for an automatic distinction between different subject groups, including patients with different neurological or psychiatric disorders.

Acknowledgment

The research was supported by the Ministry of Education, Science and Technological Development of the Republic of Serbia (contract 451-03-68/2022-14/200103).

References

[1] S. Palmis, J. Danna, J-L. Velay & M. Longcamp, "Motor Control of Handwriting in the Developing Brain: A Review", *Cognitive Neuropsychology*, vol. 34, no. 3-4, pp. 187-204, Sep 2017.

[2] R. Mergl, P. Tigges, A. Schröter, H. Möller & U. Hegerl, "Digitized analysis of handwriting and drawing movements in healthy subjects: methods, results and perspectives", *Journal of Neuroscience Methods*, vol. 90, no. 2, pp. 157–169, Aug 1999.

[3] N. Ivančević, M. Novičić, V. Miler – Jerković, M. Janković, D. Stevanović, B. Nikolić, B. M. Popović & J. Jančić, "Does handedness matter? Writing and tracing kinematic analysis in healthy adults", *Psihologija*, vol. 52, no. 4, pp. 413–435, Jan 2019.

[4] P. Drotár, J. Mekyska, I. Rektorová, L. Masarová, Z. Smékal, & M. Faundez-Zanuy, " Evaluation of handwriting kinematics and pressure for differential diagnosis of Parkinson's disease", *Artificial Intelligence in Medicine*, vol. 67, pp. 39–46. Feb 2016.

[5] P. Drotár, J. Mekyska, I. Rektorová, L. Masarová, Z. Smékal, & M. Faundez-Zanuy, "Analysis of in-air movement in handwriting: A novel marker for Parkinson's disease", *Computer Methods and Programs in Biomedicine*, vol. 117, no. 3, pp. 405–411, Dec 2014.

[6] V. Miler Jerkovic, V. Kojic, D. N. Miskovic, T. Djukic, V.S. Kostic & M. B. Popovic, "Analysis of on-surface and in-air movement in handwriting of subjects with Parkinson's disease and atypical parkinsonism", *Biomedical Engineering / Biomedizinische Technik*, vol. 64, no. 2, pp 187-194, Apr 2019.

[7] R. Mergl, O. Pogarell, G. Juckel, J. Rihl, V. Henkel, T. Frodl, F. Müller-Siecheneder, M. Karner, P. Tigges, A. Schröter & U. Hegerl, "Hand-motor dysfunction in depression: characteristics and pharmacological effects", *Clinical EEG and neuroscience*, vol. 38, no. 2, pp. 82–88, Apr 2007.

[8] N. Ivančević, V. Miler-Jerković, D. Stevanović, J. Jančić, M. B. Popović, "Writing kinematics and graphic rules in children with ADHD", *Serbian Archives of Medicine*, vol. 148, no. 7-8, pp. 462-468, Jan 2020.

[9] N. Ivančević, "Kinematic analysis of handwriting in neurological, psychiatric and neurodevelopmental disorders of childhood and adolescence", Ph.D. dissertation, Biomedical engineering and technologies, University of Belgrade, Belgrade, Serbia 2021.

[10] V. Miler Jerković, V. Kojić, M. B. Popović, "An Information and Reliability Analysis of handwriting Kinematics", 2nd International Conference on Electrical, Electronic and Computing Engineering IcETRAN, Silver Lake, Serbia, pp. 1-4. 8-11 June 2015.

[11] E. J. Smits, A. J. Tolonen, L. Cluitmans, M. van Gils, B. A. Conway, R. C. Zietsma, K. L. Leenders & N. M. Maurits, "Standardized Handwriting to Assess Bradykinesia, Micrographia and Tremor in Parkinson's Disease", *PLoS ONE*, vol. 9, no. 5, pp. 1-8, May 2014.

[12] D. Bennabi, P. Vandel, C. Papaxanthis, T. Pozzo, E. Haffen, "Psychomotor retardation in depression: a systematic review of diagnostic, pathophysiologic, and therapeutic implications", *Biomed Res Int*., pp. 1-18, Oct 2013

 ISBN 978-86-7466-930-3

Morphological parameters assessment with a depth camera based measurement system

Olivera Tomašević, Luka Mejić, Darko Stanišić, Nikolina Maravić

***Abstract*—Lately, depth cameras are being widely used for computer vision applications such as human pose estimation, activity recognition, object and people tracking, 3D mapping and localization. Possibilities for depth sensing integration in economy sectors like agriculture and healthcare services are growing as researchers are stating numerous advantages in contactless measurements done by robust low-cost depth camera systems. In this paper, we discuss an application of two different depth-sensing technologies for morphological parameters assessment.**

***Index Terms*— Morphological parameters, active depth-sensing technology, Intel RealSense.**

I. INTRODUCTION

Since computer vision has largely been concerned with obtaining 3D information from 2D images, the invention of low-cost commercial depth sensing cameras made a significant contribution to solving computer vision problems. Derived 3D depth map allowed segmentation of the scene into foreground and background, which facilitated identification and tracking of simple objects. This opened new opportunities for many practical computer vision applications such as human pose estimation [1], activity recognition [2], object and people tracking [3], 3D mapping and localization [4].

Depth maps and resulting 3D reconstructions of objects acquired in real time also enabled non-contact measurement of objects' morphological properties. Researchers have been assessing objects' static properties such as size [5] and volume [6], and dynamic such as breathing patterns [7] in conditions of clinical interest. With this application, depth sensing is likely to gain significant role in economic sectors such as agriculture and healthcare services, but also in industrial and clothing design, and ergonomics.

Namely, in [8] it was concluded that when it came to body measurement, depth camera acquired results close to real data, and as a more affordable method, it could be an appropriate alternative to high cost laser scanner. In similar fashion, in [9] the depth camera based body measurement was shown to be an efficient approach for anthropometric data collection, and in [10] it was demonstrated that low-cost depth camera based system could be used for rapid and robust tracking of body shapes and anthropometric changes in children.

Contactless measurement of body size and volume has also been described as an innovative tool for making management decisions for livestock. In [11], the authors demonstrated an accurate body measurement system based on Microsoft Kinect v2 camera, which was applied to livestock. They successfully validated the quality of generated model against manually measured body references such as height, depth, length, and girth of certain body parts. Similarly, in [12], the authors presented the measurement of body parameters such as linear and integral characteristics along directional lines and local areas, geodesic distances and perimeters of cross sections. While in [13], the measurement system was also based on Microsoft Kinect sensor, the aim was the livestock's growth assessment through the repetitive analysis of 3D models of their certain body portions.

In a similar manner, and in order to optimize the harvesting by the growth state and crop yield assessment, researchers have been measuring structural parameters of fruits and vegetables. For instance, from the segmented lettuce point clouds in [14], they extracted the volume, surface area, leaf cover area, height predictors, and correlated them to the fresh weight. Analysis showed that the calculated surface areas correlated strongly with measured fresh weight. With the similar aim, in [15] the authors used a Microsoft Kinect sensor and reported that accuracy of the 3D models of cauliflower crops deviated from the ground truth measures by less than 2 cm in diameter/height, while the fruit volume estimation showed an error below 0.6% overestimation.

When it comes to expected measurement accuracy, it immensely depends on the choice of depth-sensing technology and application context, particularly lighting conditions and working distance. Namely, depth-sensing technology has been developing for many years in several different forms. Stereo [16] may be the most basic approach for acquiring 3D depth maps. It is a "passive" depth sensing method that uses two or more standard RGB cameras, and calculates depth by finding correspondences between image points. In contrary, "active" [17] approaches use their own light sources, and can potentially overcome the limitations of passive stereo, such as large textureless surfaces and low light levels.

As revised in [18], on the market there are several representatives of state-of-the-art active depth-sensing solutions. Intel RealSense product line is one of them. It supports active depth-sensing technologies that marked the last decade: structured (coded) light (SL), active IR stereo (AIRS), and time-of-flight (TOF). In this paper, we discuss the measurement of morphological parameters using two

Olivera Tomašević is with the Faculty of Technical Sciences, University of Novi Sad, Trg Dositeja Obradovića 6, 21000 Novi Sad, Serbia (e-mail: olivera.tomasevic@uns.ac.rs).

Luka Mejić is with the Faculty of Technical Sciences, University of Novi Sad, Trg Dositeja Obradovića 6, 21000 Novi Sad, Serbia (e-mail: mejic@uns.ac.rs).

Darko Stanišić is with the Faculty of Technical Sciences, University of Novi Sad, Trg Dositeja Obradovića 6, 21000 Novi Sad, Serbia (e-mail: darkos@uns.ac.rs).

Nikolina Maravić is with the Faculty of Technical Sciences, University of Novi Sad, Trg Dositeja Obradovića 6, 21000 Novi Sad, Serbia (e-mail: nikolina.maravic@uns.ac.rs).

 ISBN 978-86-7466-930-3

different Intel RealSense solutions, which we find suitable for close range applications.

The paper is organized as follows. First, we describe the acquisition system and software, then we look at the expected accuracy depending on the chosen device, and in the end, we propose methods for morphological parameters assessment based on a point cloud data.

II. THE METHOD

A. Acquisition system

Namely, Intel RealSense has produced depth cameras through three different series: SR300, D400, and L500. Each series represents a distinct depth sensing technology. What separates them is their ideal operating parameters, along with differences in how accurate the depth information is in different situations [19]. As SR300 and D400 series allow measurements of similar distance ranges, we opted to incorporate a representative of each in our acquisition system, independently.

SR305 camera is Intel RealSense's only representative of SR300 series [20], and thus it's only representative of structured light technology. The camera uses patterned light to determine depth within the scene, thus it is ideal for use in indoor, controlled lighting situations. It is also intended for very short-range applications under one meter, but its operating range goes even up to 2m. It utilizes rolling shutter technology, has a field of view (FOV) of 71.5° x 55° and will provide up to 640×480 resolution depth images at 60 fps.

D435i camera is one of Intel RealSense's representatives that belong to D400 series [21]. It is based on active IR stereo, which uses stereo vision to calculate depth, but also projects an invisible infrared pattern to improve depth accuracy in scenes with low texture. Taken that it is based on stereovision, it is expected to perform equally well in both indoor and outdoor environments. It has an ideal operating range of 0.3m to 3m. It utilizes global shutter technology, has a wide field of view of 85.2° x 58°, and provides up to 1280 x 720 resolution depth images at 90 fps. Since depth camera D435 is another representative in the series that only differs in IMU presence, in the following text we will use the term D435, as equally.

For the purposes of visualization, Intel has developed specialized tools such as Intel RealSense Viewer and Intel RealSense Depth Quality Tool, but has also developed an open source SDK [22] that supports various platforms and programming languages, thus enabling us to build applications for data acquisition and processing adapted to our needs.

B. Acquisition software

Software for data acquisition on PC is written in Matlab (ver. R2021a, MathWorks, USA). It allows acquisition parameters setting, acquisition and processing, and visualization.

Acquisition parameters refer to stream configuration and depth property settings. These parameters are supported by the SDK library, which allows the configuration of the camera with a number of internal settings.

Stream configuration implies settings like stream type, stream format, stream resolution, and sampling frequency. Stream types refer to different types of data provided by RealSense devices. In order to get point cloud that contains RGB information for every data point, our software allowed acquisition of both, depth frame, i.e. data from depth sensor, and color frame, i.e. image from embedded RGB camera. These were thereafter aligned in order to get final point cloud representation of the scene. Available stream format, which identified binary data encoding within a frame, was set to a predefined value, which depended on a type of a stream.

Sampling frequency can take several different predefined values. In cases of dynamic parameter assessment, the sampling frequency value also determined the time resolution of dynamic morphological parameters. Thus, in cases when official documentation did not recommend any value that would ensure good quality depth, we set the highest possible value that still allowed depth and RGB frame alignment. The same applied to stream resolution parameters.

In order to get good quality depth data, we set specific values to a combination of depth property parameters such as depth projector power, accuracy, filter option and depth preset setting. The values were set specifically to achieve as better depth accuracy as possible.

Depth preset setting is a working mode that implies predefined settings for all the depth property parameters that official documentation offers as optimal for certain conditions. Considering that we were after high accuracy mode, if it was supported for given device, we opted for high accuracy preset.

In case of SR305 device, depth accuracy was set through the depth property parameter of the same name, which defined the number of patterns projected per frame. In case of D435 device, high depth accuracy was achieved through the high accuracy preset, which set high confidence threshold value of depth.

Intel SDK library includes post-processing filters to enhance the quality of depth data and reduce noise levels. When done in real time, it negatively affects the temporal resolution of the acquired frames, which should be taken in consideration when assessing dynamic parameters of an object.

As recommended in [23], images acquired with SR305 camera were filtered with default depth filter, which had moderate smoothing effects.

C. Expected accuracy

As said before, expected measurement accuracy immensely depends on application context, particularly lighting conditions and working distance. However, even when these conditions are met in accordance to camera specifications, 3D reconstructed model is still very likely to contain inaccurate, i.e. dimensions that differ from ground truth.

Depth error of SR305 camera is described in [23]. The systematic distance inhomogeneity in case of this camera brings two main systematic error components increasing with distance: non-planarity and depth offset. Non planarity can be explained through error map between the target plane and multiple point clouds acquired with increasing distance from the plane itself, while depth offset can be approximated by a parabolic function with a high coefficient of determination. For instance, for distance of 65 cm, depth offset is somewhat larger than 12 mm.

The error inherent in SR305 camera acquisition is perhaps best portrayed through evaluation of the error introduced in

 ISBN 978-86-7466-930-3

measuring a flat surface that compares SR305 camera model with D415 camera model from D400 series. The comparison can be found in [24]. Namely, D415 has a considerably lower error both in terms of planarity and of distance accuracy.

D435 camera is, on the other hand, a lot more similar to D415 camera - they use the same vision processor to provide RGB-D data. The main difference lays in depth quality, which is usually portrayed through RMS error - the depth noise for a localized plane fit to the depth value. Comparison between the two models can be found in [25]. Namely, the depth RMS error scales as the square of the distance away from the camera, in both cases. However, due to the wider FOV, the smaller baseline, and the smaller sensor resolution, the D435 has more depth noise at any given range. At the same time, this model benefits from having smaller minimum operation distance, which allows acquisition at shorter distances, and global, as opposed to rolling, shutter sensor, so is expected to be more accurate when dealing with dynamic scenes.

D. Data acquisition and processing

The acquisition was performed indoors under artificial lighting conditions. Chosen camera was fixed at a distance of about 50 cm from the horizontal table top on which objects of interest were placed. It was taken into account that placed object should be in the camera's field of view and that all its interest points should also be within the recommended range of distances for a given camera type.

In the case of SR305 camera, RGB-D images were acquired in resolution of 640x480, and with sampling frequency of 60 Hz, and in the case of D435, they were acquired in resolution of 848x480, and with sampling frequency of 30 Hz. Upon the start of acquisition, the first couple of frames were discarded to allow the camera time to settle.

The steps we found useful in the process of parameters extraction were the following:

- points selection within a region of interest in the point cloud so as to lower the computational recources needed for further processing steps
- potential selection of markers that would be used for parameter assessment
- potential rigid transformations so as to align the direction of markers propagation with a certain axes of the camera local coordinate system
- potential plane fitting through the table surface so as to assess camera tilt relative to the table, and perform appropriate tilt correction through rigid transformations
- calculation of the distance between markers based on Euclidean distances between the each two nearest adjacent points
- calculation of surface area in a region of interest based on Delaunay triangulation [26] of point cloud data
- extraction of cross sections defined by the markers trajectory
- calculation of the cross-section area
- in the cases of dynamic parameters assesment, tracking of marker koordinates over succesive frames

III. RESULTS

The point cloud acquisition and calculation of morphological parameters is demonstrated on the cropped RGB-D image of a human body torso. Fig. 1 contains RGB-D image acquired with SR305 (on the left), and with D435 camera (on the right), respectively.

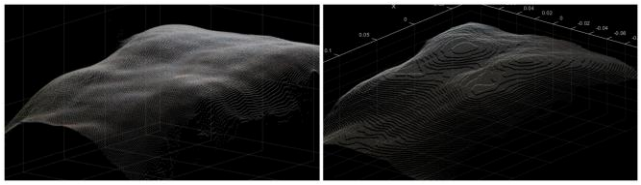

Fig. 1. Cropped RGB-D image of a human body torso captured with SR305 (on the left) and D435 (on the right).

In the case of D435, different levels of depth values are obvious. More specifically, we acquired depth maps with resolution of 1mm, which is a default depth unit of underlying vision processor. In the case of SR305, depth unit is a lot smaller (0.000125 m), thus its depth resolution is higher, as can also be noted in the figure. Other than on visual representation, these differences did not have any significant affect on parameters assessment methods. They are processed in the same manner, and results are stated in the following figures.

Fig. 2 contains example of static morphological parameters derivation based on trajectories in certain directions. Resulting cross-sections are visible in the point cloud (on the left), and isolated so that their length could be assessed (on the right). Top row refers to measurements based on SR305 camera, while bottom row refers to D435 camera. As previously stated, the cross-section lengths were estimated by the calculation of Euclidian distances between the each two nearest adjacent points.

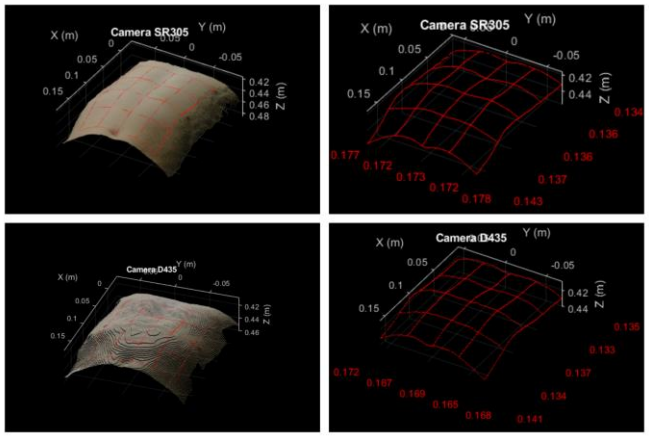

Fig. 2. Static morphological parameters derivation: cross-sections marked in a point cloud (on the left), and extracted cross-sections (on the right) along with their calculated dimensions.

Due to the anatomical planes in which they are located, these cross-sections are referred to as transverse and sagittal cross-sections, respectively. They depended on the marker positions, which were set on nipples and navel, by the user selection. Transverse cross-sections were defined based on direction on which the nipples were lying, and they were equidistantly distributed between the level of the nipples and level of the navel. Sagittal cross-sections were perpendicular with respect to them. The outermost positions of the sagittal cross-sections were left and right nipple location, respectively.

 ISBN 978-86-7466-930-3

These measurements were rounded to a precision of 1 mm. As can be seen on Fig. 2, there are certain differences in the cross-section length measurements that depend on the used camera. They are most prominent in sagittal sections and amount the most in the case of difference of 10 mm in favor of SR305 camera for the outermost left sagittal cross-section (from the perspective of the respondent). We assume that significant part of this difference lays in depth-offset error of camera SR305, which reportedly [23] takes out around 4 mm for the object distance of 400 mm, and 5.433 mm for the object distance of 450 mm.

Extracted cross-sections and their dimensions may indicate local torso characteristics. On the other hand, the object, the torso in this case could also be described globally by parameters such as surface area and volume. An example of surface area calculation is given in Fig. 3. Figure represents marked surface in the region of interest defined by the same markers that defined cross-sections: locations of nipples and navel. The area was estimated on tridimensional polygon mesh generated with Delaunay triangulation applied to the point cloud data illustrated in Fig 4. The resulting surface area is calculated upon all the areas of triangles at the base of the resulting mesh.

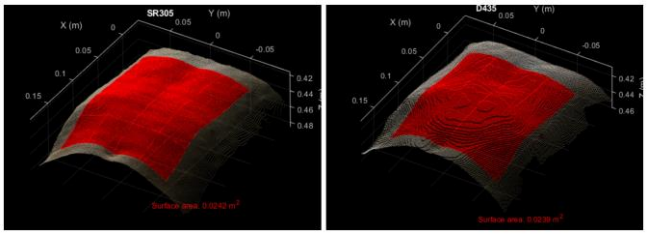

Fig. 3. Static morphological parameters derivation: marked surface in the region of interest – SR305 image (on the left), and D435 image (on the right) along with their respective results.

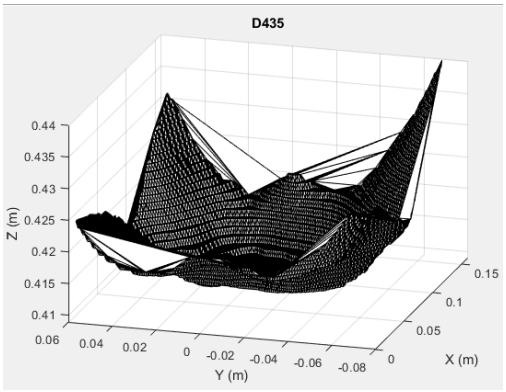

Fig. 4. Tridimensional polygon mesh calculated on the point cloud region of interest. This specific example refers to RGB-D image acquired with camera D435.

As Fig. 3 indicates, the image from SR305 camera resulted in slightly higher value of surface area parameter – 0.0242 m^2 as opposed to 0.0239 m^2 that resulted from D435 acquisition. This is in accordance with the conclusion regarding the length of the cross-sections acquired with these cameras.

Considering that demonstrated parameters can directly allow estimating of the dimensions of either torso or its parts, non-contact measurements of this type could have a purpose in clinical practice.

IV. Discussion

Results above show that visual representation of the scene did not vary significantly depending on the used camera. However, there are certain differences in their performance. Namely, results confirm the higher resolution of camera SR305 compared to D435 model (see Fig. 1). Considering that SR305 is capable of detecting depth with a higher resolution than D435, if the morphological characterization of fine details within small samples was at task, it could be expected that SR305 would be able to better reconstruct the object model, and thus would allow drawing contours that might not be visible in the acquisition with D435 camera.

On the other hand, SR305 has non-planarity and depth offset issues that contraindicate its use in precise measurement systems. As previously stated, in terms of planarity and distance accuracy, SR305 is outperformed by D400 series representatives.

When it comes to D400 series, D415 has more precision than D435. This regularity is accounted to the larger field of view of D435 camera. However, considering that D435 is better suited for dynamic scenes than D415, it could be expected that both these representatives of D400 be equally used in applications concerning morphological parameters assessment.

V. Conclusion

The aim of this study was to demonstrate derivation of morphological parameters with different depth sensing technologies. We discussed acquisition parameters that would allow good depth in static, as well as in dynamic scenes, and gave an example of static parameters calculation that could have a purpose in clinical practice.

As we discussed two different acquisition systems, we can conclude that for this type of application, one should use D400, rather than SR300 series, as it is more likely to provide sufficiently reliable measurements for the task at hand.

References

[1] Marin-Jimenez, M.J., Romero-Ramirez, F.J., Munoz-Salinas, R. and Medina-Carnicer, R., 2018. 3D human pose estimation from depth maps using a deep combination of poses. *Journal of Visual Communication and Image Representation*, *55*, pp.627-639.

[2] Park, S.U., Park, J.H., Al-Masni, M.A., Al-Antari, M.A., Uddin, M.Z. and Kim, T.S., 2016. A depth camera-based human activity recognition via deep learning recurrent neural network for health and social care services. *Procedia Computer Science*, *100*, pp.78-84.

[3] Zhou, Q.Y. and Koltun, V., 2015. Depth camera tracking with contour cues. In *Proceedings of the IEEE Conference on Computer Vision and Pattern Recognition* (pp. 632-638).

[4] Schubert, S., Neubert, P. and Protzel, P., 2017, July. Towards camera based navigation in 3d maps by synthesizing depth images. In *Annual Conference Towards Autonomous Robotic Systems* (pp. 601-616). Springer, Cham.

[5] Vo-Le, C., Van Muoi, P., Son, N.H., Van San, N., Duong, V.K. and Huyen, N.T., 2021, January. Automatic Method for Measuring Object Size Using 3D Camera. In *2020 IEEE Eighth International Conference on Communications and Electronics (ICCE)* (pp. 365-369). IEEE.

[6] Dellen, B. and Rojas Jofre, I.A., 2013. Volume measurement with a consumer depth camera based on structured infrared light. In *Proceedings of the 16th Catalan Conference on Artificial Intelligence, poster session* (pp. 1-10).

[7] Kotoku, J.I., Kumagai, S., Uemura, R., Nakabayashi, S. and Kobayashi, T., 2016. Automatic Anomaly Detection of Respiratory Motion Based on Singular Spectrum Analysis. *International Journal of Medical Physics, Clinical Engineering and Radiation Oncology*, *5*(01), p.88.

 ISBN 978-86-7466-930-3

[8] Yüksel, H. and Oktav, M.B., 2020. Analyses of body measurement with depth image data using motion capture sensor. *Industria Textila*, *71*(6), pp.530-537.

[9] Lin, Y. L., Wang, M. J. and Wang, B., 2015. Body dimension measurements using a depth camera. *New ergonomics perspective* (pp. 367-371), CRC Press/Balkema.

[10] Park, B.K., Lumeng, J.C., Lumeng, C.N., Ebert, S.M. and Reed, M.P., 2015. Child body shape measurement using depth cameras and a statistical body shape model. *Ergonomics*, *58*(2), pp.301-309.

[11] Ruchay, A., Kober, V., Dorofeev, K., Kolpakov, V. and Miroshnikov, S., 2020. Accurate body measurement of live cattle using three depth cameras and non-rigid 3-d shape recovery. *Computers and Electronics in Agriculture*, *179*, p.105821.

[12] Ruchay, A.N., Dorofeev, K.A., Kalschikov, V.V., Kolpakov, V.I. and Dzhulamanov, K.M., 2019, October. A depth camera-based system for automatic measurement of live cattle body parameters. In *IOP Conference Series: Earth and Environmental Science* (Vol. 341, No. 1, p. 012148). IOP Publishing.

[13] Pezzuolo, A., Guarino, M., Sartori, L. and Marinello, F., 2018. A feasibility study on the use of a structured light depth-camera for three-dimensional body measurements of dairy cows in free-stall barns. *Sensors*, *18*(2), p.673.

[14] Mortensen, A.K., Bender, A., Whelan, B., Barbour, M.M., Sukkarieh, S., Karstoft, H. and Gislum, R., 2018. Segmentation of lettuce in coloured 3D point clouds for fresh weight estimation. *Computers and Electronics in Agriculture*, *154*, pp.373-381.

[15] Andujar, D., Ribeiro, A., Fernandez-Quintanilla, C. and Dorado, J., 2016. Using depth cameras to extract structural parameters to assess the growth state and yield of cauliflower crops. *Computers and Electronics in Agriculture*, *122*, pp.67-73.

[16] Flusser, B.Z.J.: Image registration methods: a survey. Image Vis. Comput. 21(11), 977–1000 (2003)

[17] Krig, S., 2014. *Computer vision metrics: Survey, taxonomy, and analysis* (p. 508). Springer nature.

[18] Giancola, S., Valenti, M. and Sala, R., 2018. *A survey on 3D cameras: Metrological comparison of time-of-flight, structured-light and active stereoscopy technologies*. Springer Nature.

[19] Intel® RealSense™ Depth and Tracking Cameras, 2019. *Which Intel RealSense device is right for you? (Updated June 2020)*. [online] Available at: https://www.intelrealsense.com/which-device-is-right-for-you/ [Accessed 15 May 2022].

[20] Intel ® RealSense TM Depth Camera SR300 Series Product Family Datasheet Intel ® RealSense™ Depth Camera SR305, Intel ® RealSense™ Depth Module SR300 Revision 002, 2019. [online] Available at: https://www.intelrealsense.com/wp-content/uploads/2019/07/RealSense_SR30x_Product_Datasheet_Rev_002.pdf [Accessed 15 May 2022].

[21] Intel ® RealSense TM Product Family D400 Series Datasheet Intel ® RealSense™ Vision Processor D4, Intel, n.d. [online] Available at: https://www.intelrealsense.com/wp-content/uploads/2022/04/Intel-RealSense-D400-Series-Datasheet-April-2022-v2.pdf?_ga=2.226817501.1950346234.1651486981-1661064436.1599063643 [Accessed 15 May 2022].

[22] Intel® RealSense™ Depth and Tracking Cameras, n.d. *Intel RealSense SDK 2.0 – Intel RealSense Depth and Tracking cameras*. [online] Available at: https://www.intelrealsense.com/sdk-2/.

[23] Carfagni, M., Furferi, R., Governi, L., Servi, M., Uccheddu, F. and Volpe, Y., 2017. On the performance of the Intel SR300 depth camera: metrological and critical characterization. *IEEE Sensors Journal*, *17*(14), pp.4508-4519.

[24] Carfagni, M., Furferi, R., Governi, L., Santarelli, C., Servi, M., Uccheddu, F. and Volpe, Y., 2019. Metrological and critical characterization of the Intel D415 stereo depth camera. *Sensors*, *19*(3), p.489.

[25] Intel® RealSense™ Developer Documentation, n.d. *Tuning depth cameras for best performance*. [online] Available at: https://dev.intelrealsense.com/docs/tuning-depth-cameras-for-best-performance.

[26] www.mathworks.com. n.d. *Delaunay triangulation in 2-D and 3-D - MATLAB*. [online] Available at: https://www.mathworks.com/help/matlab/ref/delaunaytriangulation.html [Accessed 15 May 2022].

 ISBN 978-86-7466-930-3